Final Report

Project Title: CREST: Center for Renewable Energy Science and Technology

Project Period: October 1, 2009 to November 30, 2011

Date of Report: March 20, 2012

Recipient: The University of Texas at Arlington

Award Number: DE-FG36-08GO88170

Working Partners: None

Cost-Sharing Partners: University of Texas at Arlington

Contact: Dr. Richard E. Billo. (richard.billo@uta.edu)
Dr. Krishnan Rajeshwar (rajeshwar@uta.edu)

DOE Managers: Paul Bakke, Uriel Trujillo

Table of Contents

Project Objective *3*

Task 1: Extraction of Hydrogen from Lignite and Conversion to Synthetic Crude *4*

Subtask 1.1: Catalytic Extraction of Hydrogen and Conversion **4**

Subtask 1.2: Electrochemical Extraction of Hydrogen and Conversion **12**

Task 2: CO_2 Conversion *14*

Subtask 2.1: Reduction of Carbon Dioxide Using Homogeneous Catalysts **14**

Subtask 2.2: Reduction of Carbon Dioxide Using Heterogeneous Catalysts **26**

Task 3: Integration of H_2 Extraction, CO_2 Conversion and Synthetic Fuel Processing *35*

Task 4: Bench-scale Modifications and Pilot Plant Design *38*

Task 5: Project Management and Reporting *39*

Project Spending *40*

Project Objective

The DOE project addressed an approach to the hydrogen economy by researching hydrogen generation from low cost domestic fossil fuel sources. Specifically, the CREST research team developed new processes for extracting hydrogen from southwestern lignite for the production of clean synthetic fuels such as synthetic crude oil that is free of sulfur, carbon dioxide and other pollutants that can be shipped to nearby Texas refineries and power plants for development of transportation fuels and power generation. Research was also undertaken to convert any potential by-products of this process such as CO_2 to useful chemicals and gases which may be recycled and used as feedstock to the synthetic fuel process. Finally, to ensure the proposed process is functional beyond bench scale, a detailed design of a pilot plant was completed. The overall project was divided into five tasks including a management task as outlined below.

Task 1: Extraction of Hydrogen from Lignite and Conversion to Synthetic Crude

Subtask 1.1: Catalytic Extraction of Hydrogen and Conversion

Objective:

The objective is to explore innovative processes for the co-production of hydrogen from low cost Texas Lignite Coal by performing proof of concept experiments and developing benchscale reactors for demonstration. Our objective will be to increase the yields for hydrogen from the lignite and to lower the cost of the process.

Background:

Work performed on last year's award focused on the production of oils from lignite using three processes. The first process tried was a simple destructive distillation approach where the coal was pyrolyzed in a nitrogen atmosphere. The process produced low viscosity soluble oil, flammable gases, and a char that contained fixed carbon and various minerals. The gases were found to contain large amounts of methane and carbon monoxide with small amounts of carbon dioxide. It is reasonable to assume these gases could be reformed into hydrogen and carbon dioxide with a suitable reactor and catalyst. Furthermore, the literature has shown that adding certain metal salts to the lignite may increase the gas yields by volatizing the fixed carbon. The combination of catalyzed pyrolysis and a reformer based on a microreactor may lead to economical production of hydrogen from lignite.

Results:

The first activity completed in this task was the literature review that focused on the catalytic gasification of lignite. We specifically wanted to identify additives that can increase the gas yields at lower temperatures, are low in cost, and can be applied in low concentration. The compounds we identified will be tested for catalytic activity.

We installed a new thermogravimetric analyzer (TGA) that will allow us to rapidly screen the catalysts. The TGA has been used to perform proximate analysis of coal samples from Jewitt, TX. The results were compared with those obtained by Standard Labs, Inc. and were found to have good agreement. Gases were collected from the pyrolysis of lignite at 450^{o}C and tested by gas chromatography. The composition of the gases was 66% CH_4, 24% CO, and 10% CO_2. This gas will then be reformed into Syngas that can be used for fuel synthesis, or shift to produce more H_2.

Alkali metal carbonates have been reported as promising catalysts for coal gasification (Yeboah, Y. D., Y. Xu, et al. *Carbon* **2003**, 41(2), 203-214). In our initial screen, we mixed lignite coal samples with from 0 to 50% Na_2CO_3 by mass in 10 % increments and subjected the samples to pyrolysis under a N_2 atmosphere. The results are shown in the figure 1.1.1 below and reveal that addition of 10% Na_2CO_3 does promote the gasification of coal at temperatures in excess of 500 C. Interestingly, addition of greater amounts of this salt does not further assist the gasification process and can actually hinder it.

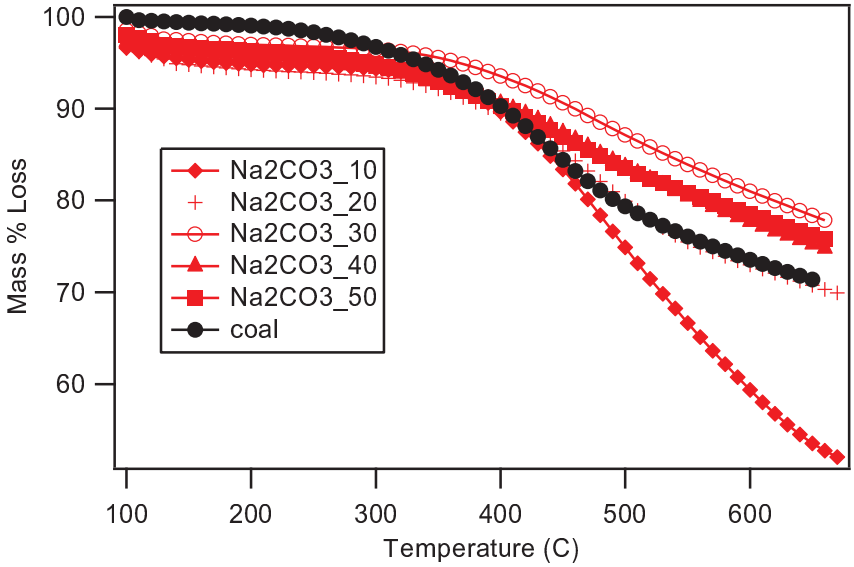

Figure 1.1.1: TGA results for first catalyst

We then examined the effects of transition metal salts in the divalent state. For a typical run, we mixed a sample of the lignite coal and a 10% by mass addition of the M(II) salt in an aqueous slurry which was then dried in an oven at 110 for 3 h to completely dry. TGA analysis under a N_2 atmosphere was used to determine the mass loss upon heating the solid samples. Greater mass loss at lower temperature is the preferred result indicating gasification of the solid. Straight pyrolysis at 450 C yields the following gasses and %: 66% CH_4, 24% CO, and 10% CO_2.

The data for the TGA runs are shown in Figure 1.1.2 below. $FeCl_2$, $CoCl_2$, $NiCl_2$, $CuCl_2$, $ZnCl_2$ were all examined with the best results seen for $CuCl_2$ closely followed by $FeCl_2$. In both of these cases, we observe a mass loss of ~ 20% at 400 C which increases to 45 % for $FeCl_2$ and 55% for $CuCl_2$ at 600 C.

In order to determine the effect of the anion, we examined $Fe(NH_4)_2SO_4$ in place of the chloride salt for Fe(II). Surprisingly, the effect was quite dramatic, with an increase in total sample gasified at 600 C from 45 % for $FeCl_2$ to nearly 60% for the sulfate salt. The effect of oxidation state was examined by using Fe(III) in the form of $FeCl_3$ in place of $FeCl_2$. As can be seen, the $FeCl_3$, has little effect at all on the gasification of the lignite and is comparable with adding no catalyst at all.

Mixtures of the salts were examined to see if there are any possible cooperative effects. A mixture of 5% $FeCl_2$ and 5% $CuCl_2$ gave results intermediate of the pure compounds suggesting no cooperative effects.

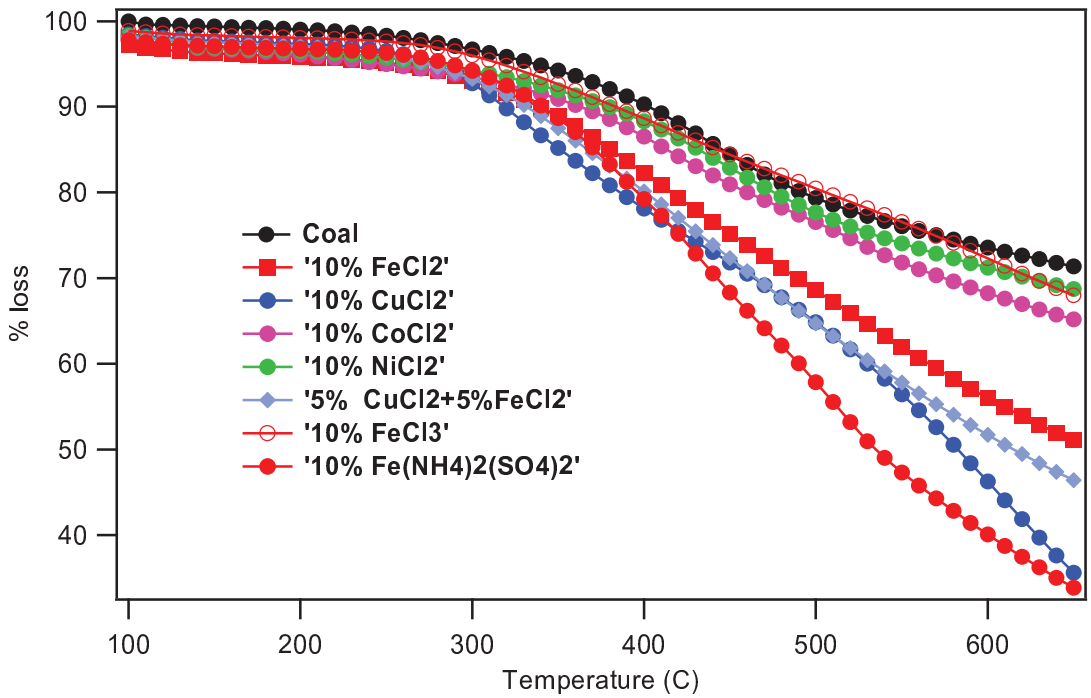

Figure 1.1.2: Results from TGA test with transition metal catalyst

Our next approach was to improve the catalytic activity of these Lewis acids by the addition of a Bronsted acid, H_2SO_4. As seen in Figure 1.1.3, the addition of H_2SO_4 alone yields an appreciable amount of gasification (60% at 600 C) and starts evolving gas products at lower temperatures (ca. 220 C) than seen with the transition metal catalysts alone which start at ca. 320 C. Importantly, a combination of $FeCl_2$ and H_2SO_4 show an incredible enhancement in gasification activity at temperatures as low as 200 C. This synergistic behavior shows that nearly 40 % of the lignite can be gasified at temperatures below 300 C which corresponds with the volatile percent composition of this sample (33%) and indicates that even some of the fixed carbon is gasified under these modest conditions.

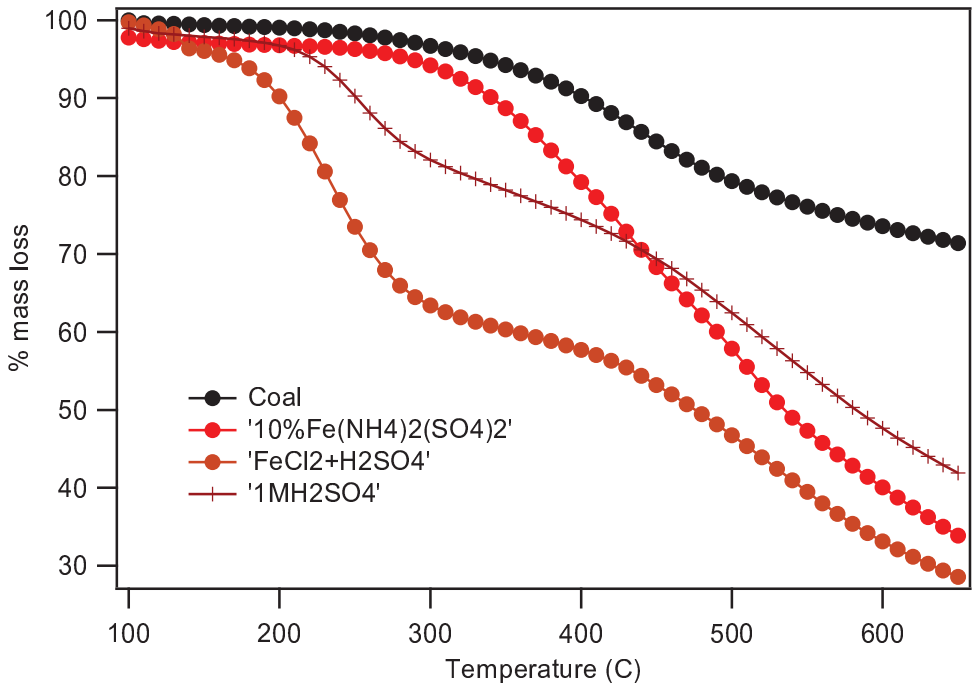

Figure 1.1.3: Results from TGA test with addition of Bronsted acids

We further examined the catalytic activity of the three previous best gasification catalysts: $CuCl_2$, $FeCl_2$, and $Fe(NH_4)_2SO_4$. A 10% by mass addition of these salts were shown to be superior in comparison with a number of other simple metal salts including: Li_2CO_3, Na_2CO_3, K_2CO_3, $NiCl_2$, $CoCl_2$, $ZnCl_2$, and $FeCl_3$. Gasification products are typically a mixture of three gases; CH_4, CO and CO_2 in an ~ 6:3:1 ratio.

The salts of Cu(II) and Fe(II) were the most productive for Lignite gasification at the lowest temperatures. In the next study, we examined the effect of using small molecule complexes of Cu(II) and Fe(II) in liu of the simple metal salts. Our previous work had established that the anion in the M(II) salt had a significant effect on the catalytic activity with sulfate, SO_4^{2-}, being superior to Cl^-. We reasoned that a bidentate ligands such as 2,2'-bipyridine (bpy) or neocuprin (neo) would keep the M(II) ion from complexing to exogenous ligands in the Lignite and still keep open coordination sites. We examined, $Cu(bpy)Cl_2$, $[Cu(bpy)_3]Cl_2$, $Fe(neo)Cl_2$, and $[Fe(bpy)_3]Cl_2$ and the TGA results are shown in Figure 1.1.4.

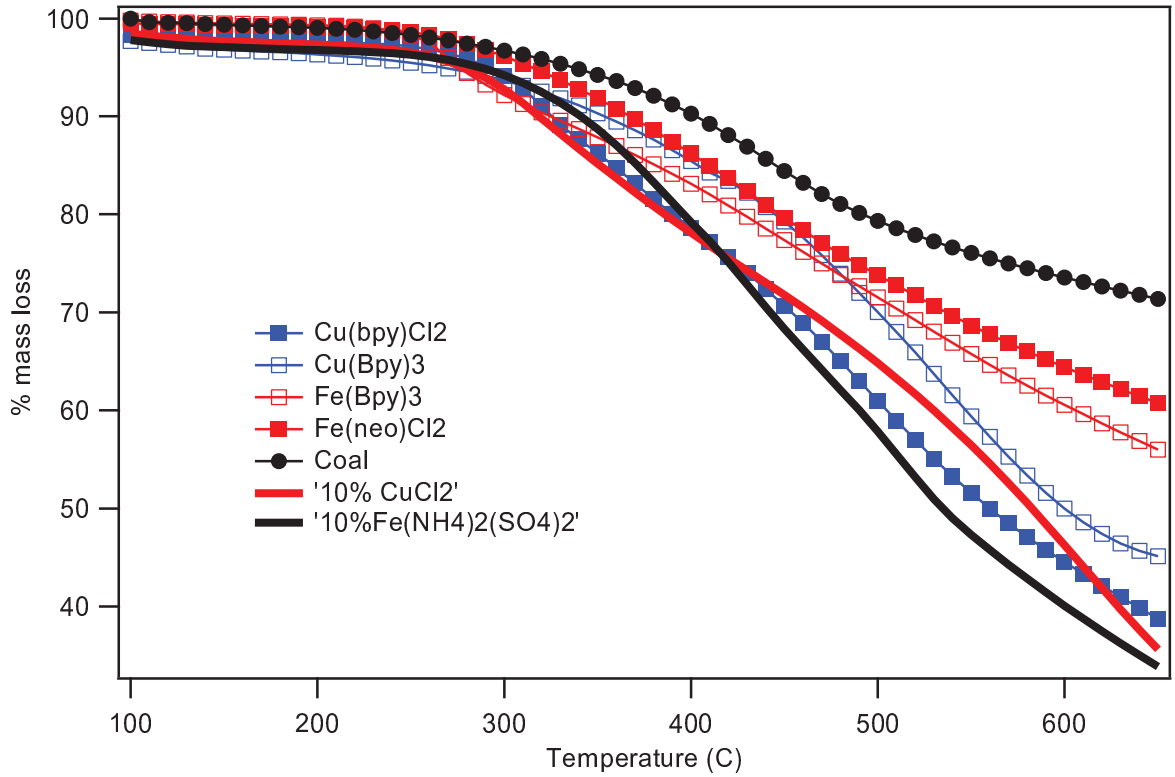

Figure 1.1.4: Results from TGA test with addition of catalysts

While the $[Cu(bpy)_3]Cl_2$ complex performed slightly better than $CuCl_2$ (thick red line), the effect was not significant enough to justify the extra expense of using a complex over a simple salt. For the Fe(II) complexes, neither performed better than the simple salt, $Fe(NH_4)_2(SO_4)_2$ (thick black line). With these results, we abandoned further complex chemistry.

In addition to studying catalysts for enhancing the production of gases, including H_2, at lower temperatures, we also worked on the development of a simple continuous flow reactor for gasification/pyrolysis.

During the first year of the project, we developed a tubular batch reactor for the pyrolysis of lignite. The goal was to maximize the yield of liquids, though the same reactor design could be used for gasification when combined with a catalyst. The small diameter of the tube (less than 1.0 inch) allows for rapid heating. A more practical design would allow for continuous operation to minimize the number of heating/cooling cycles. During the first quarter we designed a continuous flow reactor (shown in Figure 1.1.5) and fabricated a prototype. This prototype was constructed and tested in the second quarter.

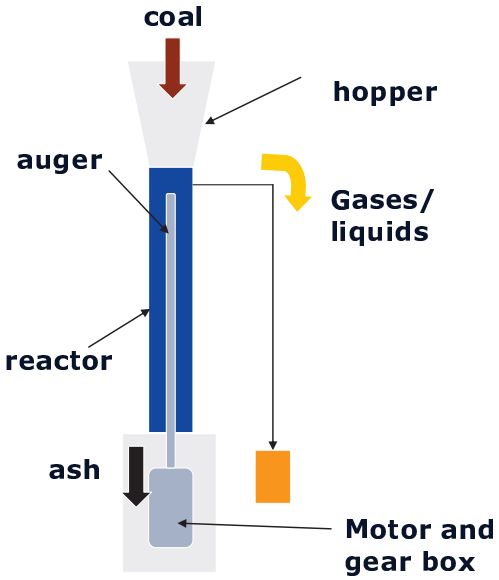

Figure 1.1.5: Tubular continuous flow reactor for pyrolysis

An augur and a motor drive system with a gear reduction unit were designed and fabricated (Figure 1.1.6).

Figure 1.1.6: Depictions of Reactor Components

These components were combined with a tubular reactor with an electric heater, insulation, feed funnel, and a water condensing unit. The assembled reactor is shown in Figure 1.1.7.

Figure 1.1.7: Assembled Reactor

The oil condensed from the pyrolysis vapors is captured in a trap flask as shown in Figure 1.1.8.

Figure 1.1.8: Assembled Reactor

After testing, the reactor tube developed cracks and eventually failed. We replaced the defunct copper tube with a steel one which proved to be much more durable. The difference in thermal conductivity has thus far remained inconsequential. Clogging was limited by using larger granules of coal, and the porosity of these grains provided the extra benefit of allowing more moisture to escape. A mesh filter was added to the condensation tube to prevent coal from combining with the oil vapors, resulting in a higher quality product.

One issue we faced was finding options to better control the flow rate of the coal. The helical pitch of the first auger was too great, allowing gravity to force more coal through than desired. A different auger was implemented to correct this. We also had to improve the gear box to avoid slippage of the gears when high torque was required to turn the auger.

These improvements allowed for testing for longer durations than we were able to achieve with previous configurations. During the testing, we discovered that the inherent moisture in the lignite leads to difficulty in operating our reactor continuously. While the lignite travels from the funnel to the reactor tube, it is gradually heated pasted the boiling point of the water in coal. The water is released as steam, which travels back up the reactor. Though some is released through the outlet and captured in the trap, the majority travels into the nozzle connecting the reactor to the funnel. There the water condenses and forms a coal/water mud that blocks the passage and prevents the lignite from flowing down.

The student operator had to continually break this blockage by moving a long metal rod up and down. We then considered design changes that would fix this problem. Several ideas were considered and tried, but the most cost effective and robust solution was to extend the auger up into the nozzle and partially into the feed funnel. This was achieved using the existing auger by shortening the length of the steel reactor tube. By doing this, the potential flow rate of the reactor was reduced by more than 60%. A longer auger can be custom made if this approach seems to be feasible.

As the overall coal liquefaction project evolved, we realized the need to produce of larger quantities of pyrolysis oil (> 1.0L per day) instead of gasifying the coal. The continuous flow reactor difficulties lead use to investigate using batch reactors that could handle larger coal capacities.

Thus, an alternative pyrolysis batch reactor was developed to process lignite on the order of ten pounds per run. The reactor is composed of a 1.25 gallon steel canister with a removable top. This allows for rapid loading and unloading. Heating is provided by electrical power. A 120V internal heater (approximately 1200 W) was designed and fabricated at UTA to provided rapid heat transfer to the lignite particles in the reactor. A nickel alloy heating wire is wrapped on the outside of the reactor to prevent condensation and reflux on the reactor walls. Mineral wool is used for high temperature insulation. The top of the reactor is connected to a series of collector traps and condensers for separating the oils and gases produced during the reaction. The assembled reactor is shown in Figure 1.1.9.

A typical run involves heating the reactor contents to 550^{o}C in the span of one hour. The temperature is held until all the volatile matter within the coal is driven off. This is typically three hours for a seven to eight pound batch. Approximately 200-300 mL of oil can be collected, depending on the batch size and moisture content.

Figure 1.1.9: Pyrolysis batch reactor

Over the course of the project, the new batch reactors have been used 3-4 times per week over the span of several months with few problems. The lignite feedstock worked well with our reactor design as it is easy to load and unload. The pyrolysis of subbituminous coal was attempted twice using one reactor to gauge the suitability of this process with that type of coal. A small amount of oil and water was produced compared to the lignite. After each run, we found the carbon and mineral residue left in

the reactor had fused into a coke-like porous solid that was very difficult to remove. We concluded that the pyrolysis reactor must be significantly redesigned for use with higher grade coals due to this coking problem.

Subtask 1.2: Electrochemical Extraction of Hydrogen and Conversion

Background and Objectives:

- Texas lignite is rich in water content and thus hydrogen. Electrolysis is an important pathway to generate clean energy from coal since the hydrogen thus produced can be either burned or used in a fuel cell to generate electricity.
- The optimization of the Texas lignite electrolysis process with two main objectives: 1) to generate hydrogen with less energy than in water electrolysis and 2) to understand the mechanism of coal electrooxidation in order to enhance the process efficiency.

Results:

We have shown that the electrolysis of Texas lignite is an efficient method to electrochemically generate H_2 with significantly less voltage than water electrolysis. To further increase the efficiency of the coal electrolysis, we have used a photo-Fenton like process which depends on the combination of Fe(II)/Fe(III) ions and light energy to assist the coal electrolysis. The irradiated anode compartment consisting of a stainless-steel electrode in contact with an aqueous acidic media containing Texas Lignite coal and dissolved Fe(II)/Fe(III) ions performs at higher currents than in the absence of light irradiation. The higher anodic currents then enhance hydrogen formation in the dark cathodic compartment made of a Pt wire electrode in aqueous acidic media. Photochemical reactions in the anodic compartment result in the reduction of Fe(III) to Fe(II) and production of hydroxyl $^{\bullet}OH$ radicals. The ability of lignite coal to capture hydroxyl radicals maximizes the amount of H_2 that can be generated at a Pt cathodic compartment. In the absence of lignite coal, the $^{\bullet}OH$ radicals attack Fe(II) ions converting them back into Fe(III) ions, and hence, diminishing the amount of Fe(II) available for the electrochemical reaction. We have analyzed and discussed these data in a recent submitted manuscript published in the *Electrochemical and Solid-State Letters (see Publication # 1 below).*

Moreover, acid digestion and oxidation with H_2O_2 were investigated as chemical pre-treatments that could improve the generation of H_2 from coal electrolysis. Three types of coals (low, medium and high rank) and two carbon black slurries were used to evaluate the chemical pre-treatments. Among the different 1 M acids that were used in this study, namely $HClO_4$, H_2SO_4 and HNO_3, digestion of Texas lignite coal (TXLC) with $HClO_4$ was found to yield the best results. It increased the polarization time (and hence the amount of H_2 generated at the cathode) during the galvanostatic polarization experiments by 50% compared to the untreated TXLC sample. On the other hand, acid digestion of carbon black (SRC-401) adversely affected the polarization time in all cases with a maximum reduction in polarization time (50%) in the case of HNO_3. H_2O_2 treatment of medium (DECS10) and high rank (DECS21) coals did not improve the galvanostatic polarization behavior of their respective slurries, while low rank coals such as TXLC showed a moderate increase in the polarization time. This modification of the

galvanostatic polarization behavior as a result of both types of chemical pre-treatments was correlated with changes in the surface area and/or surface functional groups as well as solubilization of the inherent mineral content in the coal samples. Finally simultaneous thermogravimetric and differential scanning calorimetric analyses afforded insights into the consequences of the chemical pre-treatments on the thermal reactivity of the coal and carbon black samples. These results were submitted as a full paper to the Journal of the Electrochemical Society and the paper is currently in press (*see Publication # 2 below).*

Publications/ Patents:

1. Aboushabana, M.; de Tacconi, N.R.; Rajeshwar, K. **"Photoelectrolysis of Aqueous Lignite and Carbon Black Slurry Suspensions"** *Electrochemical and Solid-State Letters* **2011**, *14 (10),* E31-E33.

2. Aboushabana, M., de Tacconi, N.R.; Rajeshwar, K. **"Chemical pre-treatment of coal and carbon black: Implications for electrolytic hydrogen generation and electrochemical/thermal reactivity"** *J. Electrochem. Soc.* **2012**, in press.

Task 2: CO_2 Conversion

Subtask 2.1: Reduction of Carbon Dioxide Using Homogeneous Catalysts

Objective: The development of molecular photocatalysts capable of reducing CO_2 to methanol using solar energy

Background: Given the current environmental concerns over CO_2 emissions, the capture and conversion of CO_2 into useful products could help alleviate the environmental issue and turn this cheap and common feedstock into value added products. Given the vast quantities of CO_2 released by the combustion of fossil fuels, the quantities of product produced from CO_2 would be large and therefore need be something usable in large quantity. The reduction of CO_2 to methanol addresses these issues in two ways: 1. methanol is itself a useful liquid fuel that could be used in large amounts, and 2. the reduction of CO_2 to methanol essentially closes the carbon-cycle, such that CO_2 added to the atmosphere via methanol combustion could be 'recycled' into fuel. Of course, there is a required energy input, but in this carbon-based fuel cycle, the ultimate energy source is solar energy.

Our molecular photocatalysts are based on the discovery of Bocarsley and co-workers that pyridine is an excellent electrocatalyst for the reduction of CO_2 to methanol (Seshadri, G., C. Lin, A. B. Bocarsley, *J. Electroanal. Chem.* **1994**, 372, 145-150) While the exact details of the multielectron reduction are still under investigation, it is clear that initial reduction of pyridinium (pyH^+) ion to the neutral radical ($pyH^{\cdot}$) is quickly followed by insertion of CO_2 to form a carbamate radical species. Subsequent electroreductions to the carbamate radical ultimately lead to complete reduction to methanol and regeneration of the pyridinium ion as shown in scheme 2.1.1.

Scheme 2.1.1

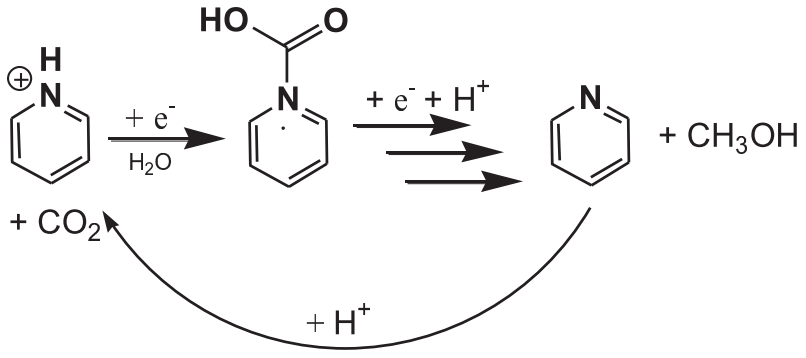

We proposed to generate the reduced pyridine functional group using the well-established photochemistry of ruthenium-polypyridyl family of coordination complexes. In particular, complexes such as $[(bpy)_2Ru(dppz)]^{2+}$ (shown in scheme 2.1.2) appear to be well-suited for this application. Excitation of this complex with visible light in the region of 400-500 nm forms an excited $MLCT_1$ state in which the dppz ligand is reduced

by 1 electron (Amouyal, E., A. Homsi, et al. *J. Chem. Soc., Dalt. Trans.* **1990**, 1841-1845. This excited state quickly relaxes to a second excited state, $MLCT_0$, in which the electron on the dppz ligand moves form a bpy-like orbital to a phenazine-like orbital as shown in scheme 2.1.2. Reductive quenching of the Ru^{3+} center traps this electron on the dppz ligand and thus has 'photogenerated' an analogue of the pyridine radical. We tested this hypothesis with three ruthenium dppz-type complexes containing pendant pyridyl groups. All three were examined for their ability to electrochemically and photochemically reduce CO_2 to MeOH.

Scheme 2.1.2

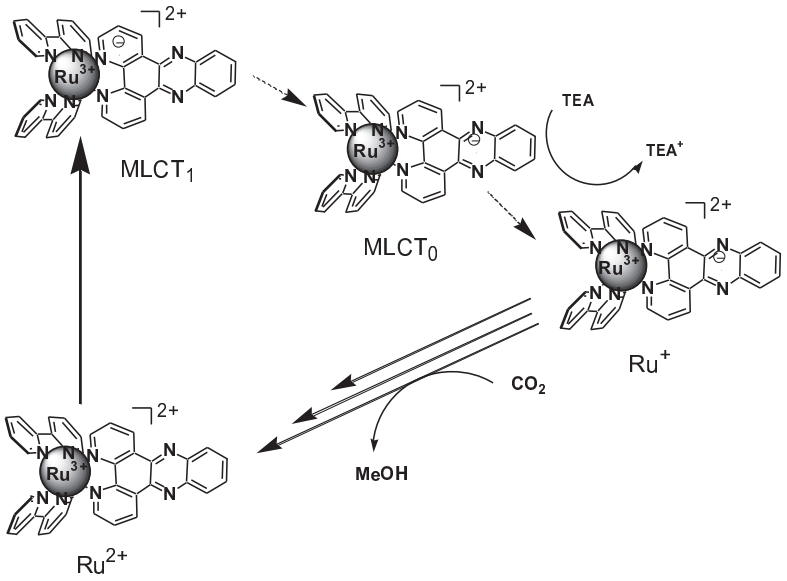

Status:

Project is complete. Over the grant period, we prepared and characterized the three photocatalysts shown below in 90% yield each. These photocatalysts are designed to photoreduce CO_2 upon photoexcitation with light in the 400-500 nm region in the presence of sacrificial reducing agents, such as ascorbic acid (AA), triethylamine (TEA), and triethanolamine (TEOA). In order to assess their capabilities, we examined the complexes redox properties with electrochemistry and the catalytic properties via electrocatalysis. The photophysics were examined by fluorimetry and photolysis experiments in the presence and absence of CO_2. Finally the complexes were examined for photocatalytic reduction of CO2 to MeOH by analyzing the reaction solution for MeOH. While it appears that we can make some small quantities of MeOH, the difficulty of detecting this analyte in a DMF based solvent system severely limited our progress.

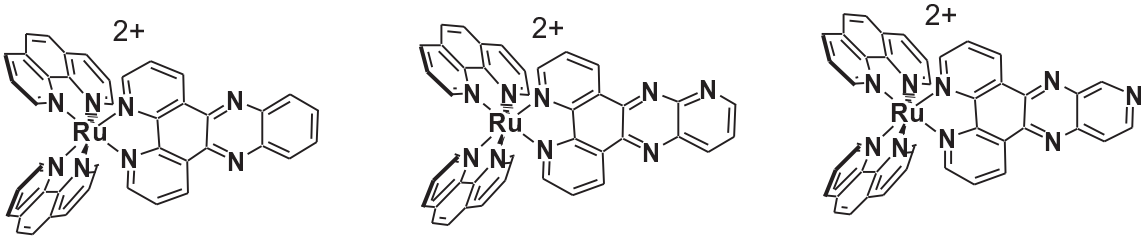

$[(phen)_2Ru(dppz)]^{2+}$ $[(phen)_2Ru(pbtp\alpha)]^{2+}$ $[(phen)_2Ru(pbtp\beta)]^{2+}$

The ground state redox properties of the complexes were assessed by electrochemical methods including cyclic voltammetry (CV) and differential pulse voltammetry (DPV), and spectroelectrochemistry (SEC). Throughout this work, we have used DMF/H_2O 99:1 as our solvent as it has been reported that the luminescence of the dppz complex is completely quenched in pure water but is re-established with increasing DMF concentration. The presence of some water is essential as it is the proton source in the reduction of CO_2 to methanol. Luminescence studies reveal that this solvent system does not appreciably attenuate the luminescent properties of any of the three complexes. This is vital for our porposed photochemical activity.

Electrochemistry

As shown in Figure 2.1.3 (left) cyclic voltammograms (CVs) of $[(bpy)_2Ru(ptpb\alpha)]^{2+}$ and $[(bpy)_2Ru(ptpb\beta)]^{2+}$ reveal reversible ligand-based reductions at -0.60 V and -0.58 V vs Ag/Ag^+, respectively. The similar irreversible redox process in the dppz complex is observed at -0.80V. As these redox processes are associated with reduction of the dppz, pbtpα, and pbtpβ ligands in their respective complexes, this is the driving force that each can use for CO_2 reduction. It is also noted that the reduction increases the basicity of the nitrogens in the ligands by 3-6 orders of

Figure 2.1.3

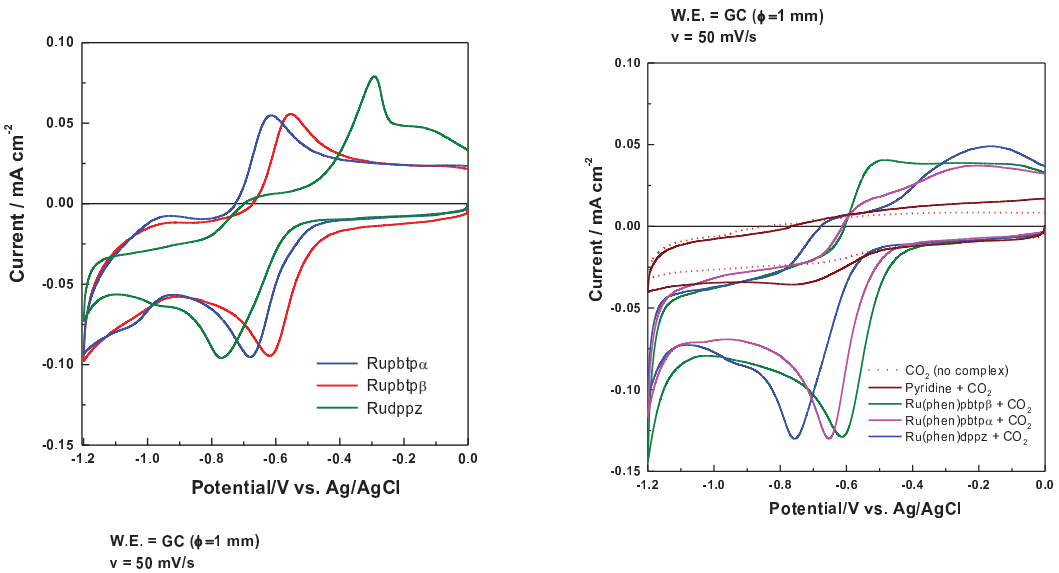

magnitude, supporting the formation of a reactive nitrogen site for CO_2 adduct formation in the form of a carbamate. Figure 2.1.3 (right) shows the changes in the CV's of these

three complexes as CO_2 is bubbled through the electrochemical solution. For all three complexes the reductive process becomes more pronounced supporting increased electron flow. The anodic process upon the return scan is now shifted and less pronounced, indicating the previously reversible process is now quasi-reversible. This is presumably due to carbamate formation. This figure also contains the CV for pyridine (brown line) for comparison and it is obvious that these complexes are far more electroactive than an equimolar amount of pyridine.

Photochemistry

The evolution of the optical spectrum of $[(bpy)_2Ru(ptpb\beta)]^{2+}$ was examined during the course of visible light irradiation in a N_2 saturated DMF solution which was 0.25 M in triethylamine(TEA) and 1.0 M in H_2O. The difference spectra are shown in Figure 2.1.4 which reveals the appearance of 4 new bands at 308, 388, 458, and 564 nm and a bleaching of another band at 344 nm.

Figure 2.1.4

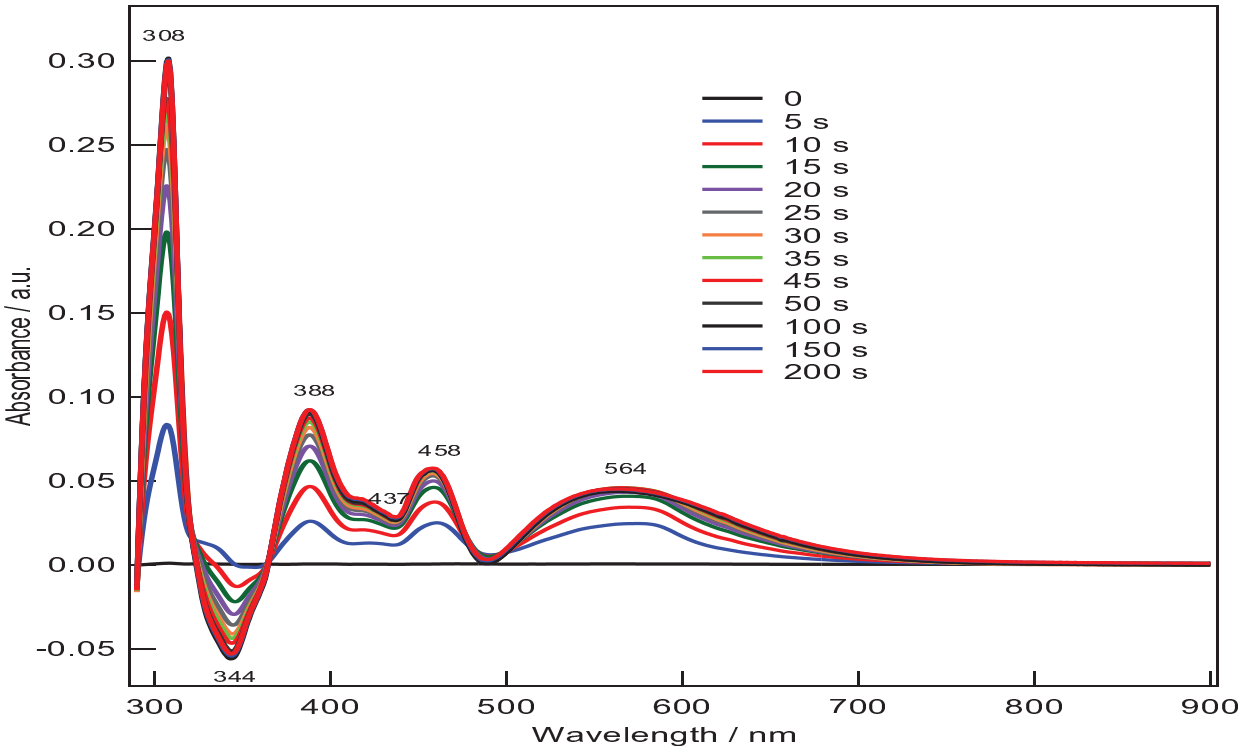

These changes are consistent with a one-electron reduction of the complex, induced by a ^{1}MLCT excitation of the Ru $\pi \rightarrow$ ptpbβ dπ band in the complex and reductive quenching of the ^{3}MLCT excited state by TEA to trap the electron on the ptpbβ ligand to form $[(bpy)_2Ru^{II}(ptpb\beta^{\cdot-})]^+$. This reduced complex is stable and is re-oxidized to the starting complex $[(bpy)_2Ru(ptpb\beta)]^{2+}$ upon introduction of air.

If the same experiment is repeated under a CO_2 atmosphere, two important observations are made. First, the resulting change in the absorption spectra is very similar to that seen for the N_2 atmosphere experiment, as seen in Figure 2.1.5 (top frame), however the reduction is observed to occur ~ 3 times faster and is finished after 30 s irradiation. Second, unlike the N_2 experiment, once the final photoproduct is formed and the light removed, slow addition of CO2 (via gentle bubbling) causes the spectrum to gradually return to the starting material over a 5 minute period.

Figure 2.1.5

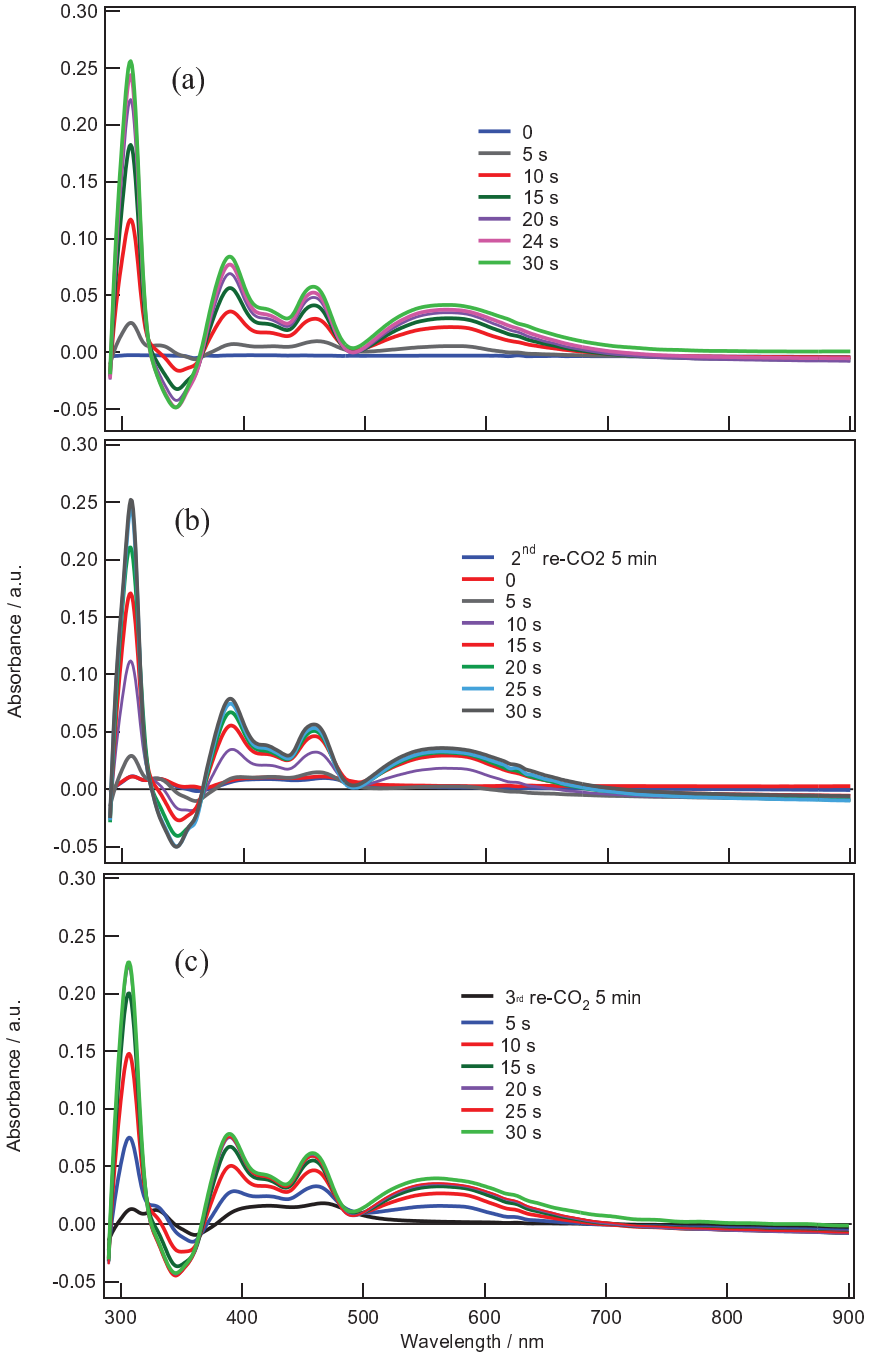

Figure 2.1.6 (frames middle and bottom) show that this photoreduction and CO_2 bubbling procedure can be repeated multiple times with little to no loss of the photocatalyst. We postulate that the 'light' photoreaction is the reductive quenching of the complex to give $[(bpy)_2Ru^{II}(ptpb\beta^{\cdot-})]^+$ and that the 'dark' reaction is the chemical reduction of CO_2 by this complex to subsequent products.

Figure 2.1.6

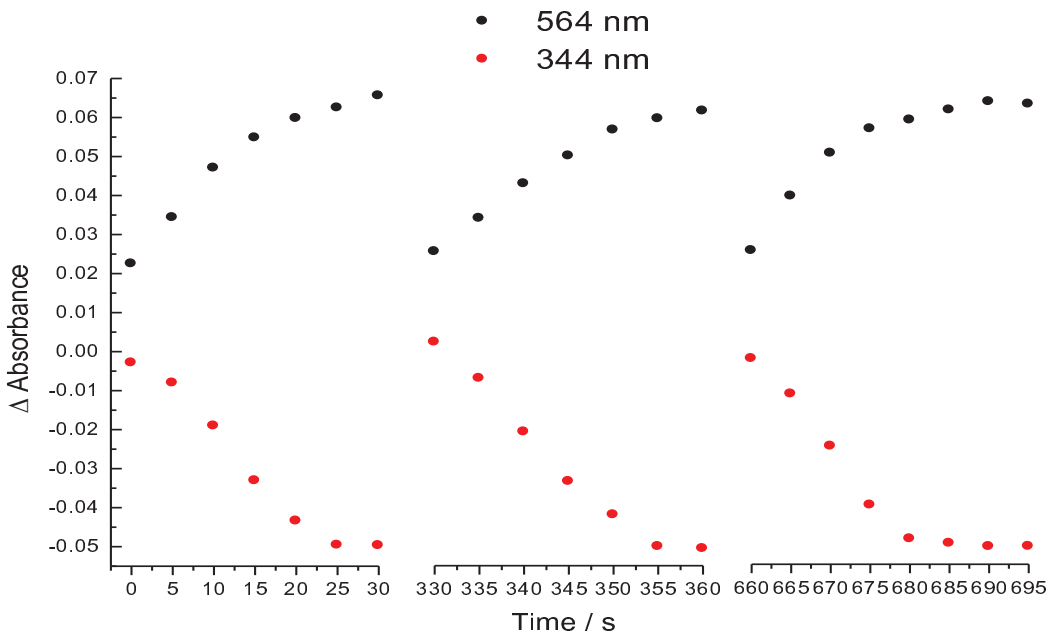

This reversibility is shown graphically in Figure 2.1.6, for the appearance of the peak at 564 nm and the bleaching of the peak at 344 nm, during the CO_2 reduction period.

These photocatalytic experiments do not reveal any informnation on the potential mechanism of CO_2 reduction, therefore we analyzed the electrochemical data by performing digital simulations to match the experimental CV data. In addition, we used SEC to follow the evolution of the absorption spectra of $[(bpy)_2Ru(ptpb\alpha)]^{2+}$ and $[(bpy)_2Ru(ptpb\beta)]^{2+}$ complexes in the presence and absence of CO_2 as a function of applied potential.

Fig. 2.1.7 shows the effect of concentration of complex $[(bpy)_2Ru(ptpb\alpha)]^{2+}$ on cyclic voltammogram profiles. The concentration was varied from 0.5 to 3.0 mM and the two peaks (labeled as $i_{c,p}$ for the cathodic and $i_{a,p}$ for anodic process respectively) are seen to progressively increase with the complex concentration. The shape of the voltammograms and the peak separation afford a Nernstian (reversible) behavior under diffusion control for this complex in the absence of CO_2. Moreover, the peak separation is not seen to be affected by the complex concentration, thus indicating that other chemical reactions such as dimer formation and/or higher aggregates are not likely occuring in this concentration range. The increase of current peaks with complex concentration follows a linear relationship and the data for the cathodic peak is shown in the inset of Figure 2.1.7.

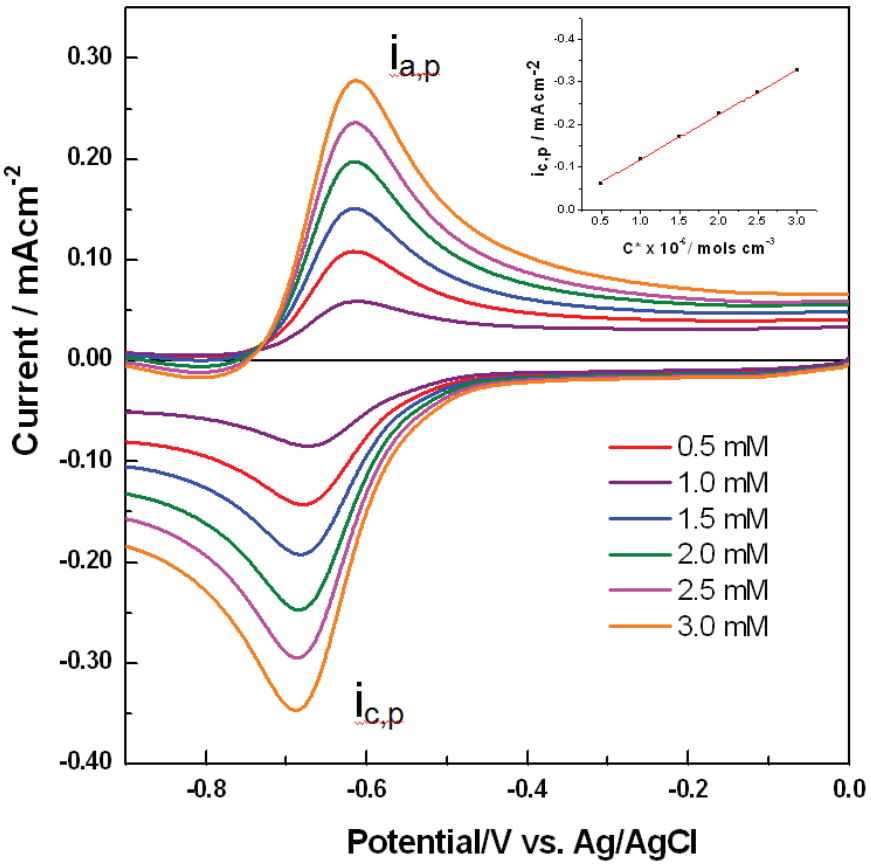

Figure 2.1.1 – Effect of concentration on the voltammetric behavior of the first electroreduction process of $[(bpy)_2Ru(ptpb\alpha)]^{2+}$ in DMF + 1 M buffered water (pH ~ 5.5). Scan rate = 50 mV/s. Working electrode = glassy carbon disk of 1 mm diameter.

The theoretical relationship of i_p vs. concentration for a reversible process is giving by

$$i_p = -0.446nF\mathbf{c}(nFv\boldsymbol{D}/RT)^{1/2} \qquad (1)$$

From the slope of the experimental $i_{c,p}$ vs. complex concentration (inset in Figure 2.1.7) and considering a one-electron reduction of the complex (n =1), a diffusion coefficient $\boldsymbol{D}$ = 3.2 x 10^{-6} cm^2/s for $[(bpy)_2Ru(ptpb\alpha)]^{2+}$ was obtained. In Eq. 1, i_p is the current density peak, n is the number of electrons per $[Ru(phen)_2pbtp\alpha]^{2+}$ unit, F is the Faraday constant, c is concentration in mol/cm^3, v is the scan rate, $\boldsymbol{D}$ is the diffusion coefficient, R is the gas constant, and T is the temperature. The obtained value of $\boldsymbol{D}$ is in good agreement with values determined for similar ruthenium complexes (de Tacconi, N. R.; Lezna, R. O.; Konduri, R.; Ongeri, F.; Rajeshwar, K.; MacDonnell, F.M. *Chem. Eur. J.* 11 (2005) 4327).

The voltammetric behavior of $[(bpy)_2Ru(ptpb\alpha)]^{2+}$ and $[(bpy)_2Ru(ptpb\beta)]^{2+}$ complexes in the presence of CO_2 is compared in Fig. 2.1.8. Purposely the runs were performed at a lower scan rate (5 mV/s that those in Fig. 2.1.1 to enhance the reaction of the first reduced product of the respective complex with CO_2. It is worth noticing that both profiles are similar in shape although $[(bpy)_2Ru(ptpb\beta)]^{2+}$ is peaking at less negative potentials than its analog $[(bpy)_2Ru(ptpb\alpha)]^{2+}$ indicating a more facile interaction with CO_2 for the first complex. In both cases, the formation of a reactive nitrogen site in the pbpb (either α or β) ligand for CO_2 adduct formation in the form of a carbamate is expected. Figure 2.1.8 also shows that a neat increase of current is occurring at potentials more negative than -1.1 V for both complexes indicating that a next electron uptake is also a possible center for photocatalytic CO_2 reduction. This point is important in the view of the photochemical reduction of CO_2 as the ^{1}MLCT excitation of the Ru $\pi\rightarrow$ ptpb dπ band in any of the complexes and reductive quenching of the ^{3}MLCT excited state by TEA could trap the electron on the ptpb ligand to form $[(bpy)_2Ru^{II}(ptpb^{\cdot-})]^+$ either in the bpy structure of the ptpb or at the farther N of the structure. The two different locations in the ptpb ligand might work properly in the photochemical reaction. In relation to the returning positive-going scan in Fig. 2.1.8, it is clear that anodic currents are much smaller than those shown in the absence of CO_2 in Fig. 2.1.7 and pointing out to a chemical reaction of CO_2 with the reduced product of any of the complexes.

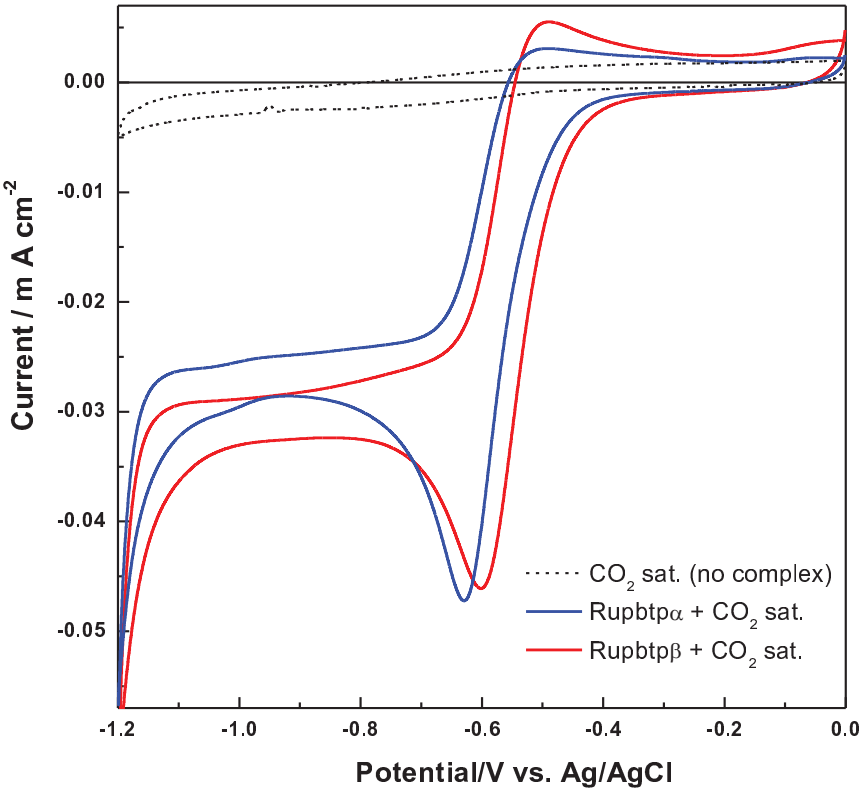

Figure 2.1.8 – Comparison of the voltammetric behavior of $[(bpy)_2Ru(ptpb\alpha)]^{2+}$ and $[(bpy)_2Ru(ptpb\beta)]^{2+}$ in CO_2 saturated solution. Scan rate = 5 mV/s. The voltammogram of CO_2 in the absence of any complex is shown in black dot line. Other experimental conditions as in Fig. 2.1.1.

For the mechanistic aspects of the electrochemical reaction, digital simulation was performed for the case of a catalytic system that involve a first reversible one-electron step follows by a catalytic reaction as indicated below:

$$\mathbf{O} + e^- = \mathbf{R} \qquad (2)$$

R + C = **O** (3)

In expressions (2) and (3), **O** and **R** are the respective oxidized and reduced species linked by a reversible electron transfer and C is a species that reversibly react with the reduced **R** species to regenerate the initial **O** species. In our case, C corresponds to CO_2, **O** to the ruthenium complex and **R** to its first reduced product respectively. Figure 2.1.8 shows digital simulations of different voltammetric profiles using BASi DigiSim v. 3.03 simulation software and considering the steps given by Eqs. (2) and (3). The different profiles were simulated under different values of the catalytic chemical reaction (3). In the absence of CO_2 (red trace in Fig. 2.1.8), i.e. considering that the rate constant for the forward direction (k_f) in Eq. (3) is zero ($k_f = 0$), a cyclic voltammogram resembling those shown in Fig. 2.1.1 is obtained as expected when one-electron reversible process is occurring without any following chemical reaction that uses the reduced **R** product. At variance, the three green profiles were simulated with an equilibrium constant for reaction (3) of 1.0×10^{10} and k_f values of 1, 6 and 20 s^{-1} respectively. Thise voltammetric profiles show that as the k_f is higher, the cathodic current increases and the respective anodic component decreases. Observe that a nice resemblance to the behavior of experimental curves of Fig. 2.1.7 is obtained corroborating the electrochemical mechanism proposed.

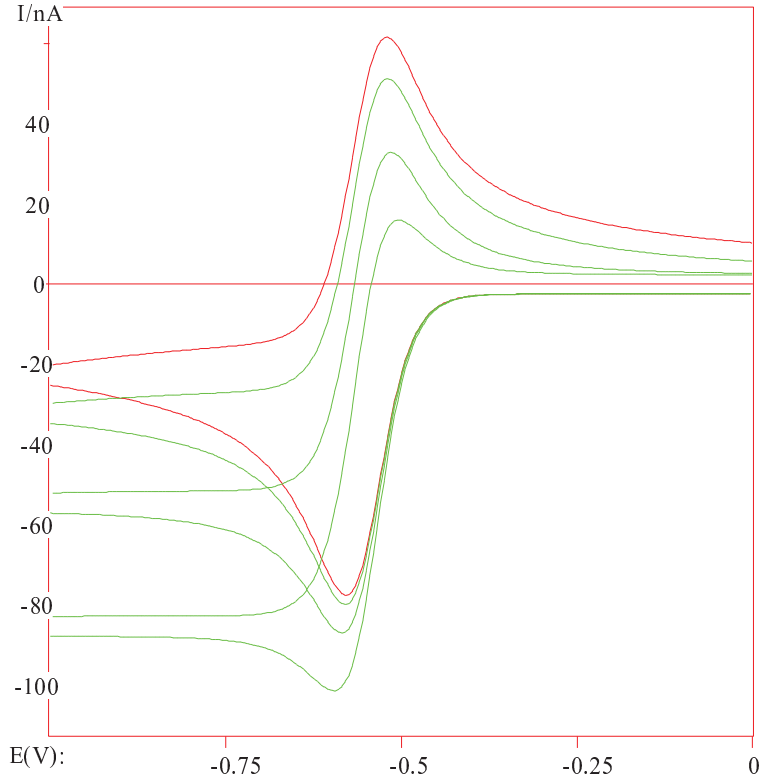

Figure 2.1.3 – Digital simulation of cyclic voltammograms according to the mechanism showed in Eqs. (2) and (3). Red trace is for the chemical reaction with forward rate constant $k_f = 0$ and the other three green curves are with progressively higher values of k_f (1, 6 and 20 s^{-1} respectively) .

Figure 2.1.9 shows differential reflectance δR/R profiles as a function of potential during a negative (0 to -1.2 V, left side) and positive (-1.2 to 0 V, right side). The δR/R changes were recorded as response to a small sin potential perturbation of 11 hz and 50 mV superimposed on a slow potential scan. δR/R profiles as in-phase and out-of phase components (positive and negative contributions in the y-axis) were obtained at 565 nm (absorption of the monoreduced $[(bpy)_2Ru^{II}(ptpb^{\cdot-})]^+$ species) and in the absence and presence of CO_2. Observe that in the absence of CO_2 (blue line) there are two lobules located at ca. -0.6 V, one in the first quadrant and other in the second that correspond to the reduction and oxidation of the complex respectively. No any other spectral signal is obtained in the rest of the potential window. However in the presence of CO_2 in the DMF solution (red trace), the lobules characterizing the $[(bpy)_2Ru^{II}(ptpb^{\cdot-})]^+$ are seen smaller than in the absence of CO_2 and thus corroborating that the amount of $[(bpy)_2Ru^{II}(ptpb^{\cdot-})]^+$ at the electrode interface is decreasing due to the catalytic reaction (3). More evidence comes when little amount of buffered water is added to the media (black trace) indicating that the carbamate is easily formed in the presence of protons.

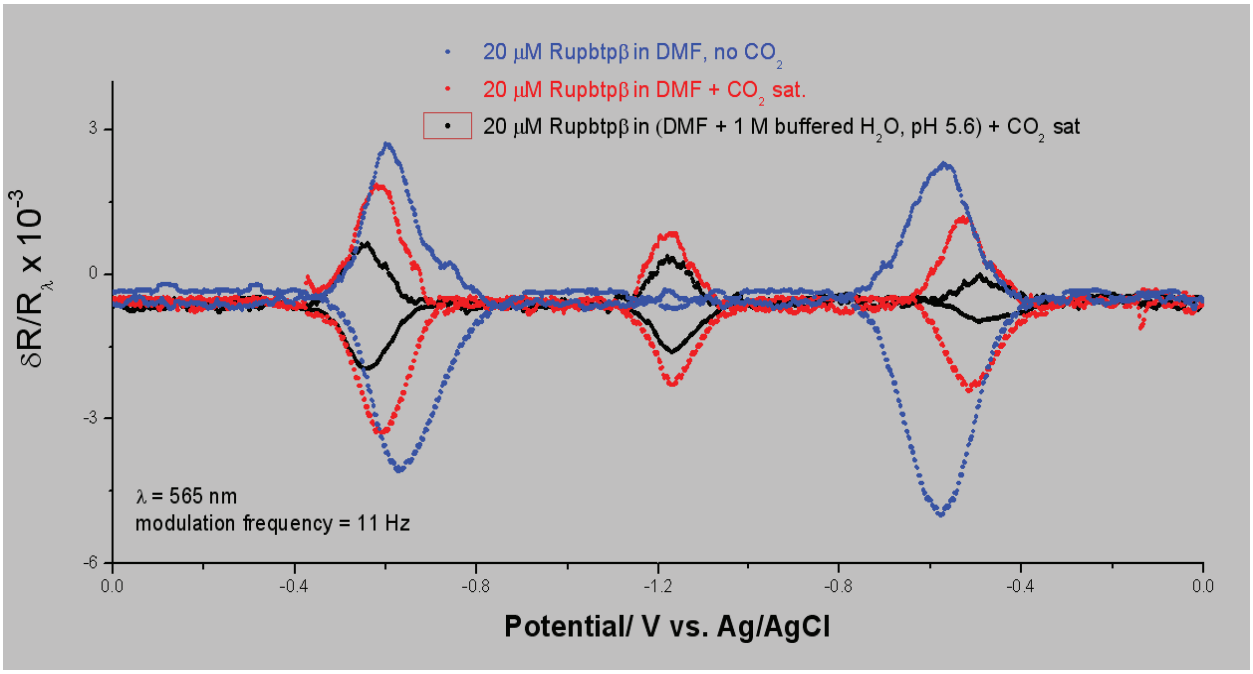

Figure 2.1.9 – δR/R profiles at 565 nm as a function of a cyclic potential scan (potential axis presented unfolded with the switching potential, -1.2 V, at the center of the axis) for 20 μM $[(bpy)_2Ru(ptpbβ)]^{2+}$ complex in the absence (blue line) and in the presence of CO_2 (red line without water and black line with water). The cyclic potential scan was performed at 2 mV/s with a superposed sin potential wave of 11 Hz and 50 mV. Working electrode was a mirror-polished Pt disc.

Methanol Production by Photochemistry

While the photochemical and electrochemical data clearly reveal catalytic CO_2 reduction, the nature of the reduced products is unknown. We have set up several photochemical reduction experiments using $[(bpy)_2Ru(ptpbα)]^{2+}$ and $[(bpy)_2Ru(ptpbβ)]^{2+}$ as photocatalysts and developed GC techniques for the determination of the small

molecule products. Difficulties with solvent (MeCN or DMF) interference or signal swamping made these results difficult to interpret unambiguously.

In a typical experiment, a water jacketed reaction vessel of 50 mL total volume was filled with ~25 mL MeCN that is 1.0 M H_2O, 0.20 M TEOA, and 100 μM Ru complex. The solutions are degassed and then placed in a homemade photochemical reactor in which blue light irradiation of wavelength 470 nm is provided by ultra bright diode array lamps. Samples of both the headspace and solution are collected at various time periods and subjected to gas chromatographic (GC) analysis for product detection.

The gas chromatograph used was a SRI Multigas #3. This GC has many features including a 10 port valve for 2D gas chromatography and two detectors, a thermal conductivity detector (TCD) and a flame ionization detector (FID). It was configured with a Haysep DB packed column with a length of 3 m and used N2 as a carrier gas. While preliminary results are done using a single column, resolution of the peaks will be possible using a second column and the 10 port valve.

We had to switch from DMF to acetonitrile as the reaction solvent as the DMF proved to be too difficult a solvent to cleanly resolve via GC. This is a result of the high boiling point of DMF and its decomposition as the temperature in the GC approached its boiling point of 153 C. Acetonitrile was a little easier to work with but stil presented certain difficulties.

We developed a method for the separation of the solvent, co-reactants and products as described below. Method 1: Starting at 110 C, a temperature ramp of 1 C/minute temperature was done immediately after sample injection to a final temperature of 150 C. Retention times were as follows: carbon monoxide, 0.80 min.; methane, 0.88 min.; methanol, 5.8 min.; formaldehyde and formic acid, 8 min. The overlay of the various analytes in the GC is shown in Figure 2.1.4. Further separation is possible using this GC by stopping the flow of the Haysep column and passing the peaks that need better separation through a separate column. Investigation into the limit of detection of the methanol in the acetonitrile system shows that the limit of detection using the FID is equivalent to 0.1 turnovers of the catalyst as shown in Figure 2.1.10.

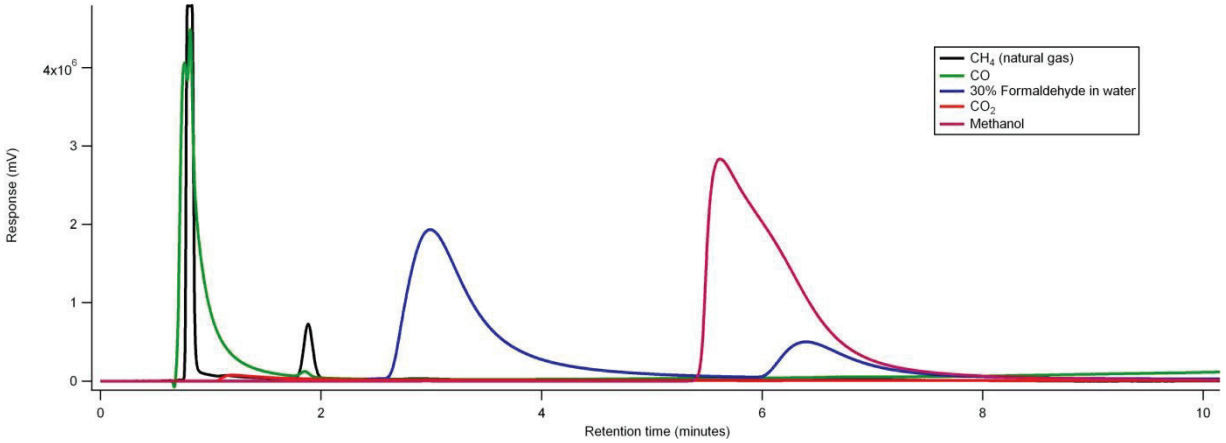

Figure 2.1.10 Standards run using 1 C/minute temperature ramp from 110 C to 150 C using a Haysep DB column. Black line is methane, domestic natural gas, green line is carbon monoxide, blue line is Formaldehyde in water, red line is carbon dioxide and the maroon line is methanol

As can be seen, the MeOH peak overlaps with some component in the formaldehyde solution, making this peak a little ambiguous. We determined the detection limits for MeOH in the GC experiment by titration and found we could detect as little as 0.1 MeOH/ Ru catalyst.

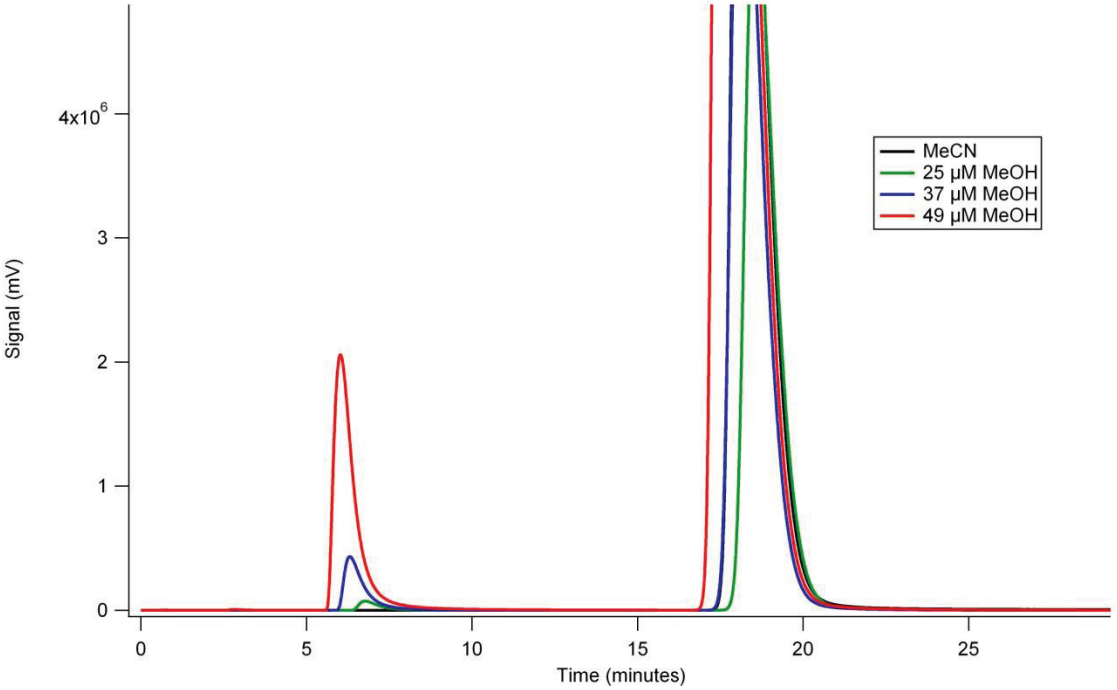

Figure 2.1.11 A titration of methanol into the system shows a low limit of detection of methanol what is equivalent 0.1 turnovers of the catalyst

Small amounts of MeOH could be detected as well as formaldehyde however the presence of small peaks in the same region for the dark reactions suggested that they may be an artifact. We postulate that the sacrificial reducing agents, AA, TEA and TEOA, which are present in relatively large amounts (0.1M), may be broken down thermally in the GC injection port and are responsible for the baseline peaks. Extended periods of irradiation showed the peaks to grow, suggestive that product is being formed, however further experiments are need to confirms this. Unfortunately the project ended before this could be completed. We are continuing on with the project using other funding sources at this time.

Subtask 2.2: Reduction of Carbon Dioxide Using Heterogeneous Catalysts

Objective: The development of heterogeneous photocatalysts capable of photoreducing CO_2 using solar energy.

Background:

The use of inorganic semiconductors to photoreduce CO_2 to useful energy-rich products such as methanol is not a new concept and dates back to the 1970s. However, the quantum developments in materials nanotechnology and new semiconductor compounds that have taken place particularly during the past decade, prompted us to re-examine the viability of this concept. To prepare semiconductor nanoparticles and use them as photocatalysts, we proposed a solution combustion synthesis procedure which has to be optimized for each particular material. Three different semiconductor materials were chosen, namely $BiVO_4$, Bi_2WO_6 and $AgBiWO_8$, all with respective band-gap in the visible spectral region paving the way to efficient utilization of the solar spectrum. All three materials were examined for their photocatalytic activity in both photoreduction and photooxidation processes.

Results:

The project is complete. During the grant period, and with the aim to develop heterogeneous photocatalysts for solar photoreduction of CO_2, we prepared three new semiconductor materials namely $BiVO_4$, Bi_2WO_6 and $AgBiW_2O_8$ for the first time by solution combustion synthesis (SCS). The synthesis variables (selection of precursors, fuels, and post-annealing temperature) were optimized for best performance under light irradiation of the resulting nanoparticles. In this way, we seek to control the important materials properties for photoactivity under visible light in the absence and presence of CO_2.

In relation to the preparative part of the semiconductor nanoparticles, we used solution combustion synthesis because is both energy- and time-efficient. The exothermicity of the combustion reaction provides the energy requirement for the synthesis and the high reaction temperatures result in finely dispersed and porous morphology for the binary ($BiVO_4$ and Bi_2WO_6) and ternary ($AgBiW_2O_8$) oxide products (**Figure 2.2.1**). The effect of a post-annealing temperature was also analyzed in its effect on the crystallinity of the compound and particle size.

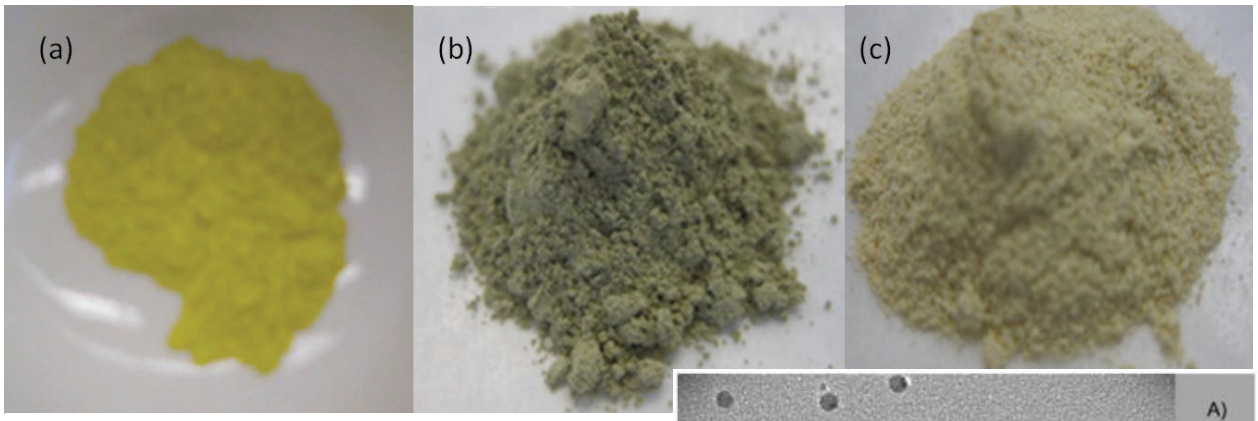

Figure 2.2.1. Appearance of the $BiVO_4$ (a), Bi_2WO
with urea as fuel.

Other advantages of SCS for the preparation are: a) simple homogeneous reaction involving just the dissolved precursors' salts and a fuel, both in water (see: Rajeshwar, K.; de Tacconi N. R. *Chem. Soc. Rev.* **2009**, *38*, 1984) and b) incorporation of multiple components as co-catalysts.

The synthesized powders were characterized by transmission electron microscopy, thermal analyses, diffuse reflectance UV-visible spectroscopy, X-ray diffraction, surface area measurements, and X-ray photoelectron spectroscopy.

Analysis of UV-visible reflectance spectra of the SCS-derived powders using the Kubelka-Munk methodology affords values for the energy band-gap of 2.2 eV for $BiVO_4$, 2.7 eV for $AgBiW_2O_8$ and 2.8 eV for Bi_2WO_6 respectively. Clearly, $BiVO_4$ is superior (relative to the other two) in terms of better overlap with the solar spectrum. However when the three materials were compared in its photocatalytic activity, the better match with solar light is not the only variable determining the photoconversion performance (vide infra).

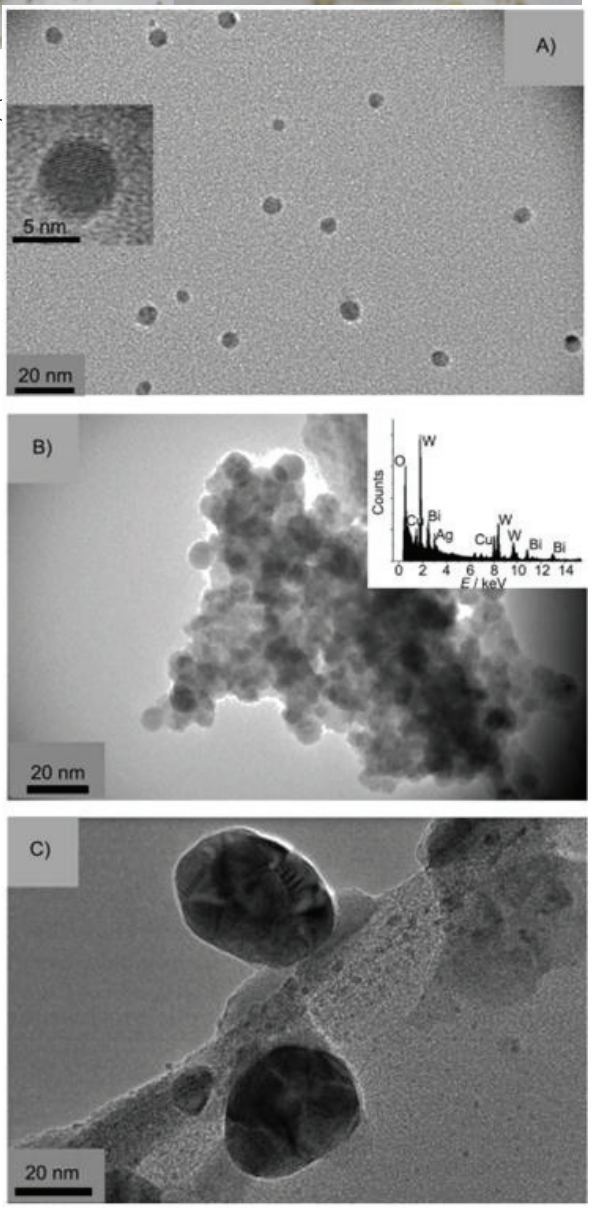

Figure 2.2.2 – HR-TEM images for $AgBiW_2O_8$ prepared by solution combustion synthesis using urea as fuel (A and B), and by SSR (C). Individual nanoparticles (A) were also found to form small aggregates (B). The EDX analysis corroborates the purity of the SCS material as the only extra element detected is Cu from the supporting mesh (insert in Figure 2.2.2B).

To exemplify the difference between the particle sizes obtained by SCS and the most common solid state reaction (SSR), representative HR-TEM images of SCS-$AgBiW_2O_8$ are compared with same compound prepared by SSR in **Figure 2.2.2.** The HRTEM images of SCS-$AgBiW_2O_8$ depict both individual spherical nanoparticles with a mean average size of 6.6±1.0 nm (**Figure 2.2.2A**), which are in accord with the particle size calculated by the Scherrer equation, and small aggregates (**Figure 2.2.2B**) as a result of partial sintering occurring during the combustion synthesis process. Besides, EDX analysis of a SCS sample (**Figure 2.2.2B**, inset) corroborates that the nanoparticles contain Ag, Bi, W and O with stoichiometric ratios as expected for $AgBiW_2O_8$. It is worth noting that even without a post-synthesis thermal anneal step, partially crystalline samples were obtained from solution combustion synthesis which underlines the advantage with this synthesis approach from an energy input perspective to add to its high time efficiency as noted above. The SSR-$AgBiW_2O_8$ showed much larger particles and required 18 hours at 800°C in the preparation. This comparison vastly demonstrates the beneficial use of SCS as method to rapidly prepare uniform and smaller nanoparticles. Consistently with the smaller particle size, the SCS samples also have a significantly higher surface area (35 $m^2.g^{-1}$) relative to the SSR counterpart (0.50 $m^2.g^{-1}$).

When the SCS-derived semiconductor nanoparticles were compared in their photocatalytic activity, clear trends appeared. SCS-$BiVO_4$ showed excellent photocatalytic performance for dye oxidation but did not perform well as photocatalyst for reduction of CO_2. The contrasting behavior for photooxidation and photoreduction reactions seems to be rooted in that the energy of the $BiVO_4$ conduction band (CB) is rather low (even lower than the requirement for solar hydrogen generation) and likewise the driving force for photoreduction of CO_2 to useful fuels (CH_4 and alcohols) was found very limited.

Although Bi_2WO_6 and $BiVO_4$ are members of the Aurivillius family, they differ in that the conduction band of the first material is located at more negative potentials than the second although with the caveat that its energy band gap is 0.4 eV higher (2.8 eV vs. 2.4 eV in its $BiVO_4$ analog (vide supra). Both nanoparticulate semiconductor materials, once optimized in the respective combustion synthesis, were found to have good photocatalytic performance for photooxidation reactions but behaving poorly for photoreductions reactions (i.e., CO_2 photoreduction and H_2 photogenetration).

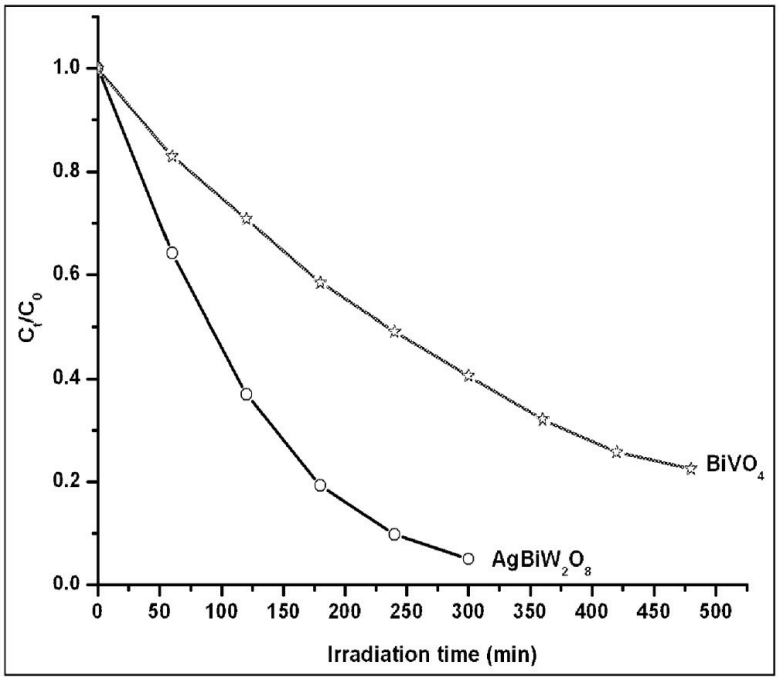

Figure 2.2.3 – Comparison of the photocatalytic activity of combustions synthesized $BiVO_4$ and $AgBiW_2O_8$ for the photodegradation of methyl orange.

The ternary SCS-$AgBiW_2O_8$ was found to be the best of the three materials

because of its high performance for both photooxidation and photoreduction reactions. A comparison of its photocatalytic activity for an oxidation reaction (specifically the methyl orange photodegradation) relative to that of $BiVO_4$ is presented in **Figure 2.2.3.** Clearly, the SCS-$AgBiW_2O_8$ nanoparticles outperform those of SCS-$BiVO_4$ in terms of proclivity to photochemically break down methyl orange in spite of the much lower overlap of the solar spectrum of $AgBiW_2O_8$ material. The photocatalysis data in Figure 2.2.3 were well fit by pseudo-first order kinetics in agreement with what is expected for methyl orange phocatalytic oxidation. The better performance of the ternary oxide is also clear in the comparison of the dye half-time is 3.61 h for $BiVO_4$ and only 1.13 h for $AgBiW_2O_8$. These comparative data underline a crucial fact: *The optical attributes only offer a partial glimpse into the suitability of a given photocatalyst for solar energy conversion or environmental remediation application.* These results are included in a recently published paper in the Journal of Nano Research (*see Publication # 1 below).*

In relation to photoreduction processes, the SCS-samples of $AgBiW_2O_8$ modified with 1 wt.% Pt were found the best of all for both photooxidation and photoreduction reactions. The resulting performance for Pt-modified $AgBiW_2O_8$ in photoreduction reaction is presented next.

Photogeneration of Syngas and Methane on Pt-Modified $AgBiW_2O_8$

Syngas (or "synthetic gas") is the name given to a gas mixture that contains varying amounts of CO and H_2. Common examples of producing syngas include the steam reforming of methane or liquid hydrocarbons, and the gasification of coal or biomass. Thermally mild (i.e., low temperature) alternatives for producing this transportable chemical fuel mixture is obviously very significant from an energy perspective. Value is even further if the production process can be driven via a renewable solar energy source from a source greenhouse gas material such as CO_2.

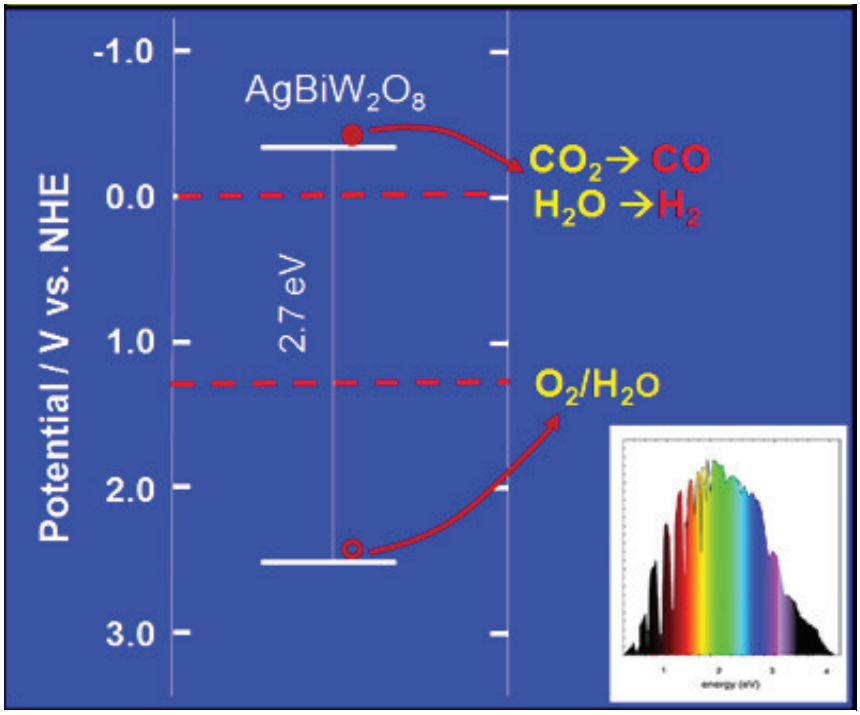

Figure 2.2.4. Energy diagram containing the position of the band edges (in a NHE potential scale) for the $AgBiW_2O_8$ semiconductor and the redox potentials for conversion of water to hydrogen, CO_2 to CO, and water to oxygen. Observe that the bandgap of this particular semiconductor is in good match with the solar light spectrum (shown in the bottom right corner).

Figure 2.2.4 shows an energy diagram containing the band edges for $AgBiW_2O_8$ (band-gap = 2.7 eV) together with relevant redox levels such as those for water and

CO_2 reduction as well as oxidation of water to O_2.

The SCS-$AgBiW_2O_8$ particles were modified with 1 mass % Pt islands using a photocatalytic procedure. The surface metal islands were used to enhance electron-hole separation during photocatalytic processes.

Figure 2.2.5 contains the high-resolution XPS data for a SCS-$AgBiW_2O_8$ sample in the binding energy regimes 3d for Ag (frame '**a**'), 4f for Bi and W (**b** and **c**), and 1s for O (**d**)] characteristic of the four elements in the compound. The Pt 4f signals for the Pt-modified $AgBiW_2O_8$ nanoparticles are depicted in **Figure 2.2.5e**. The XPS signals for the metal components are split due to spin-orbit coupling. The signals are located at 387.9 eV for silver (Ag $3d_{5/2}$), at 158.9 eV for bismuth (Bi $4f_{5/2}$) and at 35.1 eV for tungsten (W $4f_{7/2}$) respectively. These respective peaks for Ag, Bi and W are associated with Ag^+ or Ag^{2+} in an oxide structure, with Bi^{3+} also surrounded by oxygen neighbors (such as in Bi_2O_3, Bi_2O_4), and with W^{6+} in a hexagonal oxygen-bonded structure (such as WO_3, H_2WO_4). The XPS data are in accord with a layered structure for $AgBiW_2O_8$ composed of WO_6 octahedral sheets interleaved with Bi-O-Bi layers and AgO_x polyhedra. Importantly, the XPS data also confirm that there is no *free* metal formation (i.e., Ag^0, Bi^0) during SCS synthesis. For example, in the Bi binding energy regime, the Bi $4f_{7/2}$ and Bi $4f_{5/2}$ signals in Figure **Figure 2.2.5b** are located at 158.95 and

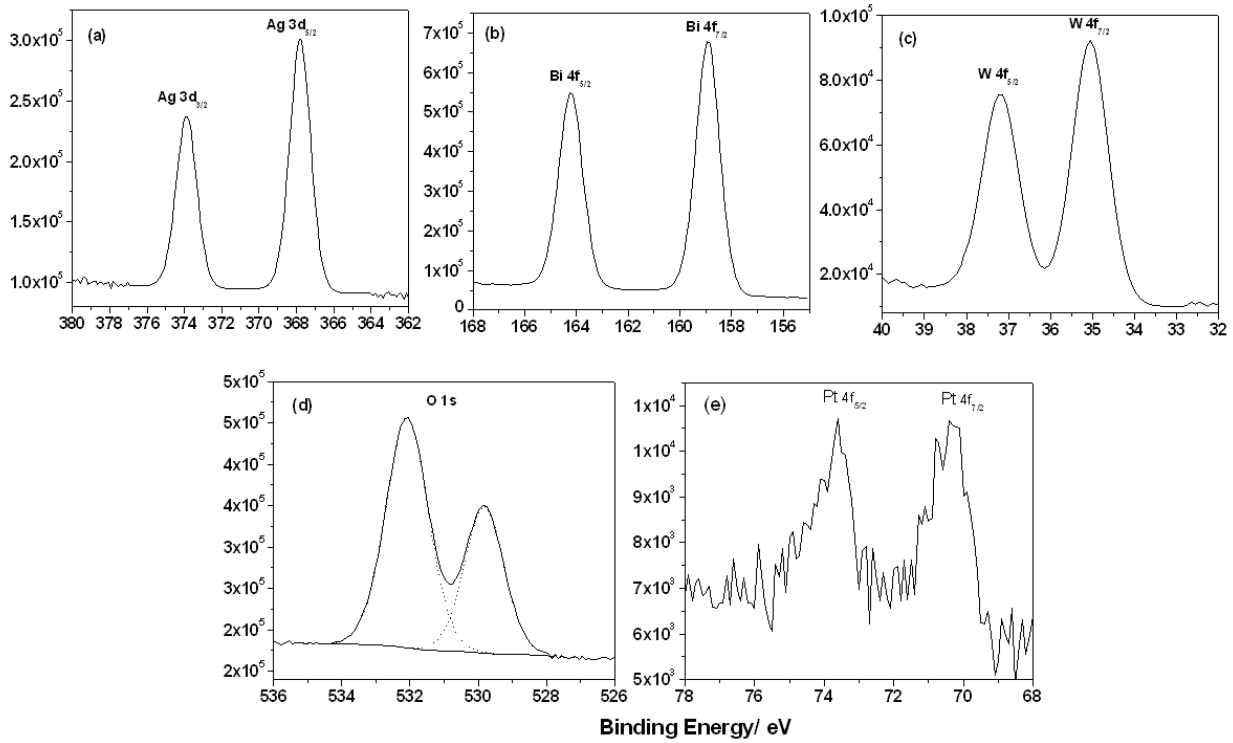

Figure 2.2.5 - High-resolution core level X-ray photoelectron spectra (ordinates in the spectra in counts per second) in the Ag 3d (a), Bi 4f (b), W 4f (c), O 1s (d) and Pt 4f (e) binding energy regimes for SCS-$AgBiW_2O_8$ (a-d) and Pt-modified SCS-$AgBiW_2O_8$.

164.2 eV; far higher in energy than the characteristic peaks for *metallic* Bi located at 156.8 eV and 162.2 eV respectively. Similar considerations apply for silver peaks as well.

In the O 1s binding energy regime (**Figure 2.2.5d**), the peak at 529.9 eV is in good agreement with that similarly reported for a bismuth tungstate structure and at variance with that for WO_3 at 530.5 eV. The other O 1s peak at 532.1 eV is assignable to residual water bound to the oxide nanoparticles and also to water molecules adsorbed on the sample surface.

Importantly, no changes were noted in the XPS profiles after use of the SCS-$AgBiW_2O_8$ sample in the dye photodegradation runs or after syngas generation attesting to the excellent photoelectrochemical stability of this oxide on band gap irradiation.

Figure 2.2.6 compares the temporal evolution (as assayed by GC) of the gaseous products for formic acid (**Figure 2.2.6a**) and acetic acid (**Figure 2.2.6b**) as the electron donor. A control with no initial Pt modification of the $AgBiW_2O_8$ powder is also included in the latter case (blue dash line). Control experiments conducted without the oxide semiconductor did not yield any of the products shown in **Figure 2.2.6** signaling that photolysis of the respective organic acid is not a factor here. It is also worth noticing that HCOOH performs as an in situ precursor for CO_2 generation (Figure **2.2.6** a). In fact, the direct electroreduction of CO_2 in aqueous media is hampered both by the low partial pressure of CO_2 in the atmosphere (3.9 x 10^{-4} atm) and by its low solubility in water (1.5 g/L at 298 K). On the other hand, formate species have high solubility in water (945 g/L at 298 K). Further, they have high proclivity for being adsorbed on oxide semiconductor surfaces and are easily oxidized by the photogenerated holes in the oxide semiconductor.

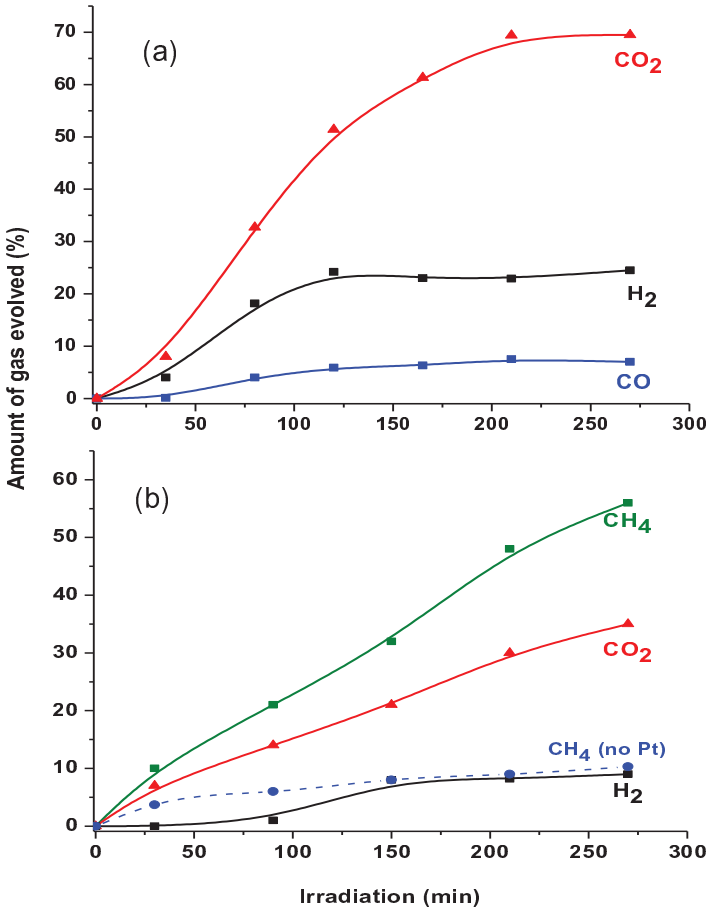

Figure 2.2.6 - Temporal evolution (as assayed by GC) of the gaseous products formed in the photocatalytic reaction of $AgBiW_2O_8$-Pt from formic acid (a) and acetic acid (b) as the electron donors. Both systems were saturated with N_2.

In both cases (**Figures 2.2.6a and b**), the photoreaction is initiated by photooxidation of the respective carboxylic acid (photo-Kolbe reaction) on the oxide photocatalyst surface. Competition by water photo-oxidation is expected only as a

minor contribution and the $^{\bullet}OH$ radicals, generated from initial hole attack on adsorbed water molecules, are most likely involved in oxidation of the carboxylic acid than in O_2 generation. H_2 photogeneration on Pt sites occurs in both cases although initial Pt modification of the oxide surface has different consequences. In the case of formic acid as the electron donor, H_2 photogeneration is completely quenched in the absence of Pt while for acetic acid (**Figure 2.2.6b**), the extent of methane photogeneration is influenced by the presence of Pt islands on the oxide surface.

The above observations can be rationalized by invoking radical intermediates that are generated on initial photo-oxidation of the organic acid. The intermediate $HCOO^{\bullet}$ radical generated in the first case (formic acid) by reaction with a photogenerated hole (in the oxide) then injects an electron into the $AgBiW_2O_8$ conduction band via the well-established current–doubling mechanism (see **Figure 2.2.7a**). The net result is formation of hydrogen atoms ($H^{\bullet}$ on Pt sites followed by subsequent H_2 formation) and

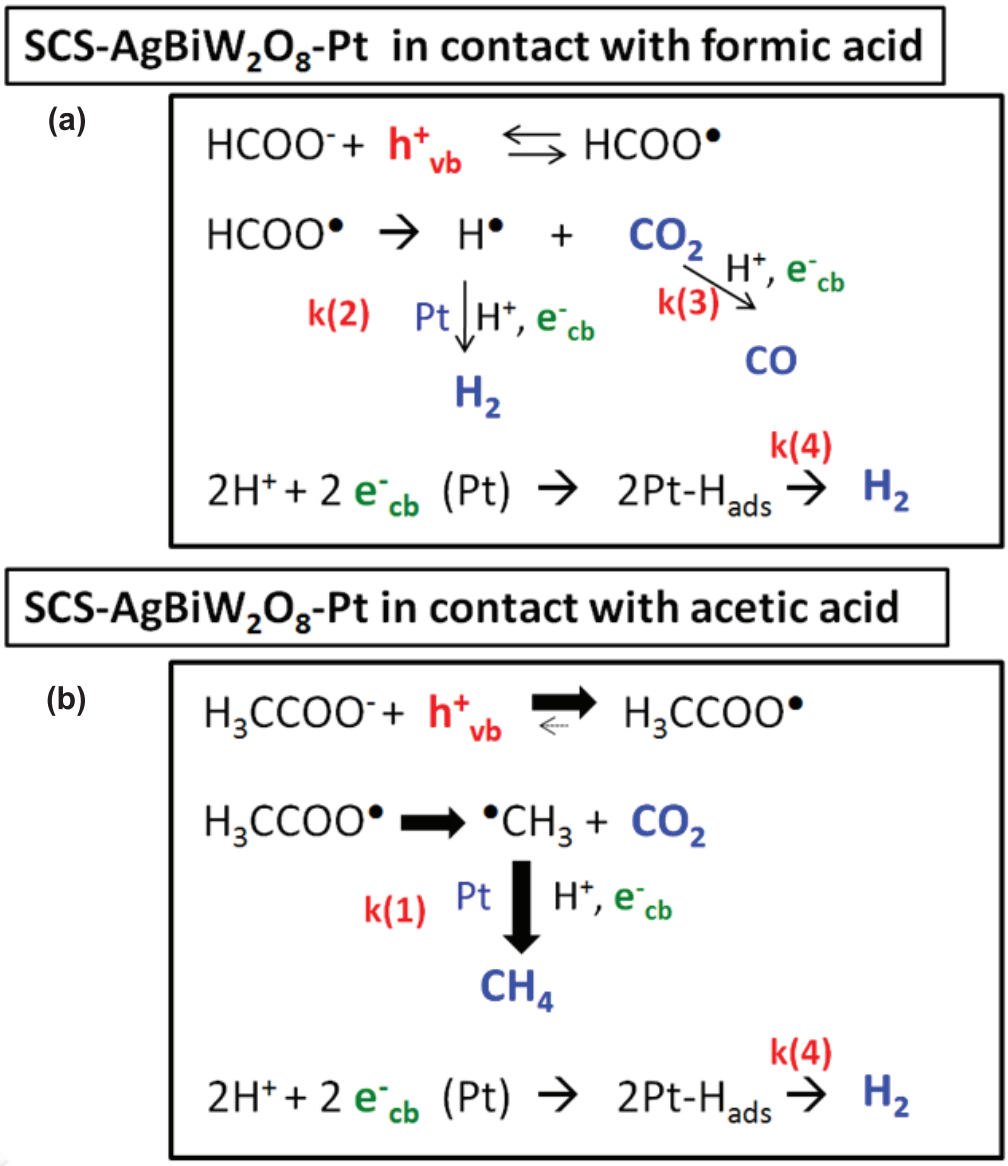

Figure 2.2.7 - Mechanistic pathways for the photocatalytic Kolbe reaction along with other reactions occurring on irradiation of Pt-modified SCS-$AgBiW_2O_8$ nanoparticles in contact with formic acid (a) and acetic acid (b) respectively.

CO_2. In the second case for acetic acid, the corresponding $H_3CCOO^{\bullet}$ photogenerated radical (formed from initial hole attack on acetate) rapidly decomposes to $H_3C^{\bullet}$ + CO_2, and then the $H_3C^{\bullet}$ radicals use the hydrogen atoms stored on Pt islands to get ultimately converted into CH_4 (**Figure 2.2.7b**). If the Pt sites are absent, the surface reaction involving the methyl radicals and hydrogen atoms would be inhibited.

What about trends in product evolution in the (*dark*) electrochemical cases for the two acids considered here? The electrochemical oxidation of carboxylic acids (Kolbe reaction) proceeds through different paths depending on the anode material. On a platinum electrode and with simple carboxylic acids such as H_3CCOOH, the Kolbe reaction (induced, for example, by galvanostatic polarization) generates hydrocarbons through a free radical sequence as follows:

$H_3CCOO^- \rightarrow H_3CCOO^{\bullet} \rightarrow H_3C^{\bullet} + CO_2$

$2\ H_3C^{\bullet} \rightarrow CH_3\text{-}CH_3$

Thus, the *normal Kolbe reaction* involves radical-radical coupling ($H_3C^{\bullet}$ coupling) as the predominant mechanism at platinum anodes while an *abnormal Kolbe reaction* almost exclusively occurs at carbon electrodes either in organic or in aqueous media generating CH_3COOCH_3. With α-substituted carboxylic acids, more complex mechanisms involving radicals and/or carbonium ion intermediates give rise to the formation of other products such as olefins, alcohols, ethers, and esters.

Interesting contrasts have been reported in product evolution for similar electrode surfaces with and without illumination. Thus ethane was observed as the dominant product on a TiO_2 *photoanode* in organic media (acetonitrile) with 0.1 M tetrabutyl ammonium perchlorate as supporting electrolyte and 0.08 M of tetrabutyl ammonium acetate as source of acetate ions. On the other hand, methane (rather than ethane) was reported on photoirradiated TiO_2-Pt nanoparticles in contact with acetic acid very similar to the observations in this study (**Figure 2.2.6b**). Methyl radical coupling (leading to ethane) is clearly favored on the massive electrode surface because of a site proximity effect.

Quantum yields for the formation of syngas (H_2+CO) and CO_2 in the formic acid solution were as follows: H_2 = 3.0 %, CO = 0.8 % and CO_2 = 4.5 %. [Chemical actinometry using an aqueous solution of 6 mM $K_3Fe(C_2O_4)_3.3H_2O$ in 1.0 N H_2SO_4 provided a calculated photon flux of 3.2 x 10^{-2} moles and thus the reported quantum yield was calculated as the percent ratio of the number of moles of product divided by the moles of photons.] The H_2:CO_2 ratio was seen to be ~ 1:1.5 for reaction times up to 1 hr, whereas it reached a ratio of 1:2.8 for reaction times higher than 3 h. Product amounts at the end of the photocatalytic runs were as follows:

$H_2 = 1.0 \times 10^{-2}$ mol/g.L

$CO = 3.0 \times 10^{-3}$ mol/g.L

$CO_2 = 2.8 \times 10^{-2}$ mol/g.L

These data are reported as the number of moles of product divided by the photocatalyst mass and liquid volume in the photoreactor. The turnover number (TON = molar amount of reacted electrons divided by molar amount of catalyst) for the photocatalytic formation of H_2 + CO (using a factor 2 to represent the number of electrons per H_2 and CO respectively) on the Pt-modified SCS-$AgBiW_2O_8$ nano-particles reached a value of ca. 4.3 after 4 h irradiation, producing 1.0 mmol of H_2 and 0.3 mmol of CO.

For the photocatalytic synthesis of CH_4 from acetic acid on Pt-modified $AgBiW_2O_8$ nanoparticles, the amount of gases generated at the end of the runs was:

$CH_4 = 1.45 \times 10^{-2}$ mol/g.L

$CO_2 = 0.92 \times 10^{-2}$ mol/g.L

$H_2 = 0.24 \times 10^{-2}$ mol/g.L

The quantum yields were as follows: CH_4 = 1.7 %, CO_2 = 1.2 % and H_2 = 0.3 %. The experimental CH_4:CO_2 ratio was found to be ~ 1.5:1 at reaction times up to 1 h, increasing slightly afterwards to 1.6:1.

Figure 2.2.7 summarizes the mechanistic paths for the photocatalytic Kolbe reaction plus other reactions occurring on irradiation of Pt-modified SCS-$AgBiW_2O_8$ nanoparticles in contact with HCOOH (Figure **2.2.7**a) and H_3CCOOH (Figure **2.2.7**b) respectively. Rate constants of the reactions associated with the photogenerated electrons are indicated as k(x) (with x = 1 to 4). The reaction product profiles are consistent with an ordering of these rate constants: k(1) > k(2) ~ k(4) > k(3). The very low amount of H_2 formed in the case of acetic acid is consistent with k(1) > k(4) which means that the photoelectrons are mainly consumed in the generation of CH_4 from the methyl radical. Importantly no C_2H_6 was found in our experiments indicating that the conduction band electrons are transferred to $H_3C^{\bullet}$ thus cancelling out the radical-radical coupling. The uptake of e^-_{cb} from Pt-modified SCS-$AgBiW_2O_8$ is much higher by $H_3C^{\bullet}$ than by CO_2 (k(1) > k(3)) and therefore no CO is observed in the data for CH_3COOH (Figure 2.2.6b). Further, k(2) > k(3) which would be consistent with the ratio, H_2 : CO ~3: 1, measured for formic acid as the electron donor.

Competition by water photooxidation is expected only as a minor contribution and the $^{\bullet}OH$ radicals, generated from initial hole attack on adsorbed water molecules, are most likely involved in oxidation of the carboxylic acid than in O_2 generation. The main product in the acetic acid solution was methane and the extent of methane photogeneration was highly influenced by the presence of Pt islands on the oxide surface. H_2 photogeneration on Pt sites occurs in both cases although initial Pt modification of the oxide surface has different consequences. In the case of formic acid as the electron donor, H_2 photogeneration is completely quenched in the absence of Pt while for acetic acid, the extent of methane photogeneration is influenced by the presence of Pt islands on the oxide surface and accounting for ca. 4 times more amount of methane.

A full paper reporting these results have been submitted for publication to *ChemPhysChem*, and it is now published as ASAP *(see Publication # 2 below).*

Publications/ Patents:

1. Rajeshwar, K.; de Tacconi, N. R.; Timaji, H. K. **"New-generation Oxide Semiconductors for Solar Energy Conversion and Environmental Remediation"** *J. Nano Research* **2012**, *17*, 185-191.
2. de Tacconi, N. R.; Timaji, H. K.; Cahnmanee, W.; Huda, M. N.; Sarker, P.; Janaky, C.; Rajeshwar, K. **"Photocatlytic Generation of Syngas Using Combustion-Synthesized Silver Bismuth Tungstate"** *ChemPhysChem* **2012**, DOI: 10.1002/cphc.201200046.

Task 3: Integration of H_2 Extraction, CO_2 Conversion and Synthetic Fuel Processing

Objective:
The objective is to integrate the catalytic gasification process and the reformer reactor developed in Task 1 with a gas-to-liquids process. A gas-to-liquids reactor will be developed for this purpose. We will investigate the use of microreactors for this purpose. The integration will be demonstrated on the bench scale.

Background:
Coal-to-liquids processes result in liquid, solid, and gaseous products. Though modern processes have addressed the use of liquid and solid phases, the gaseous byproducts are often released into the environment with little or no remediation. The majority of these are greenhouse gases, such as CH_4 and CO_2. Conversion of these gaseous byproducts to a useful liquid, such as hydrocarbons or alcohols represents an economical alternative to capture and sequestration. In Task 1, we investigate methods for reforming the gaseous products into a mixture of H_2 and CO, also known as Syngas. This Syngas can be used directly for liquid hydrocarbon synthesis using the well known Fischer-Tropsch process. This liquid can then be marketed as a fuel for vehicles with diesel or jet engines.

Results:

In the beginning of this task, we performed a conceptual design of the integration setup and the gas-to-liquids (GTL) reactor. The schematic is shown in Figure 3.1. For this reactor, we will look at microreactor designs since they allow for tight control over the temperature distribution.

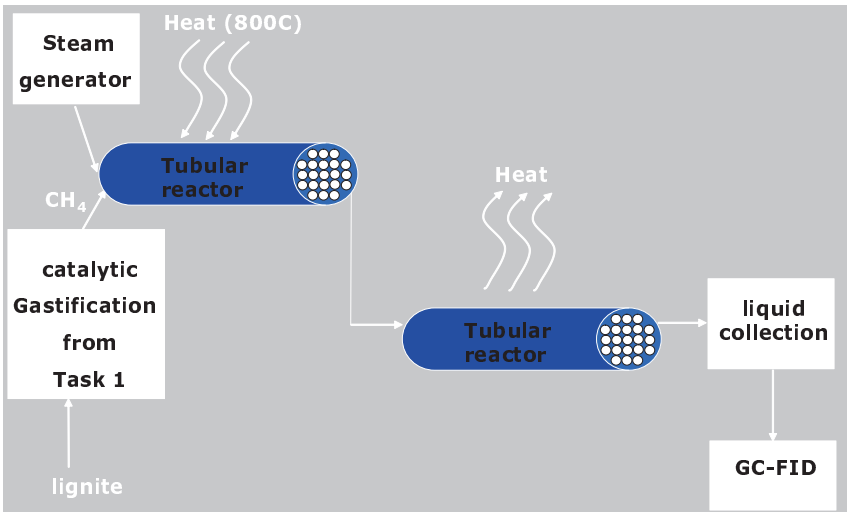

Figure 3.1: Integration of gasification, reforming, and GTL reactors

The next step focused on proof-of-principle experiments for producing liquid hydrocarbons from syngas by Fischer-Tropsch synthesis (Figure 3.2). We developed a hood scale test loop with a packed capillary microreactor. The reactor was made of stainless steel and had a diameter of 1.0 mm and length of 12.0 inches. We packed the reactor with Co-Ru on TiO_2 support. The syngas was provided by a tank containing H and CO in 2:1 molar ratio. The reactor is placed in a heated silicone oil bath that effectively provides isothermal conditions. A photo of the setup is given in Figure 3.3.

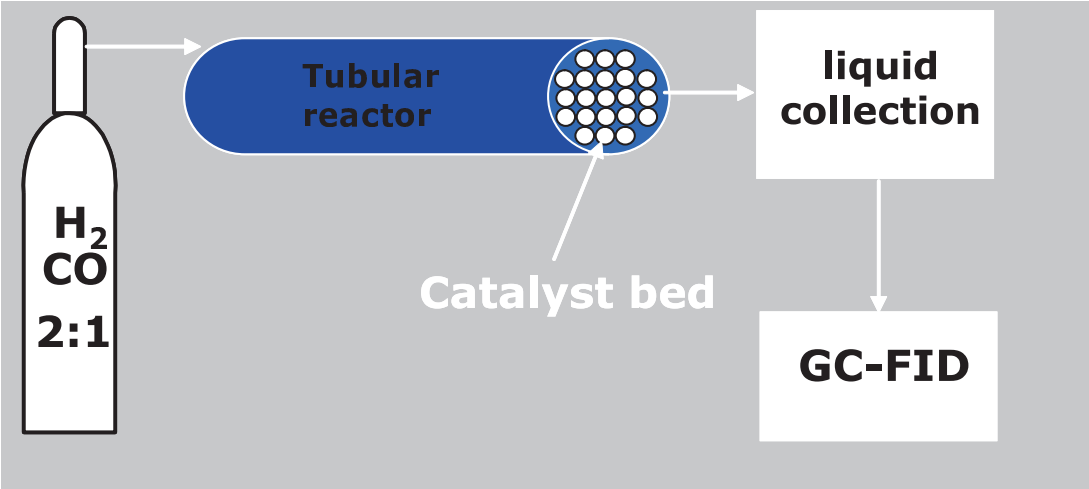

Figure 3.2: The F-T test flow diagram

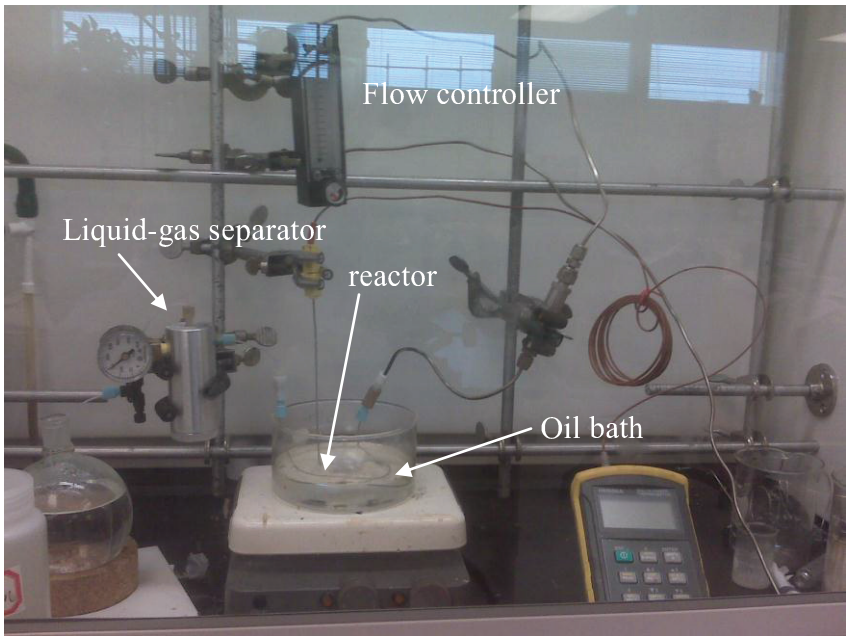

Figure 3.3: Photo of the F-T test setup

The liquids and gases are the passed to a liquid-gas separator where the liquids are collected and gases are vented to the hood. The liquids are tested using gas

chromatography to determine their composition. We tested the reactor at different temperatures (200°C-250°C) and pressures (100 psig – 150 psig). Liquids were produced for all tested conditions though the highest production rate occurred at 150 psig and 250°C.

Condensed liquid drops from vapor were observed above 180C for all pressures after heating continuously for 2 hours. Approximately 1 mL of liquids (water + liquid hydrocarbons) was obtained after four days with approximately 4 hours of run time per day. The water phase was significantly larger than the oil phase indicating that some gaseous must have been produced. We will quantify this loss in the upcoming quarter. The liquid hydrocarbons were subjected to gas chromatography testing and were found to be similar to diesel and jet fuel (Figure 3.4).

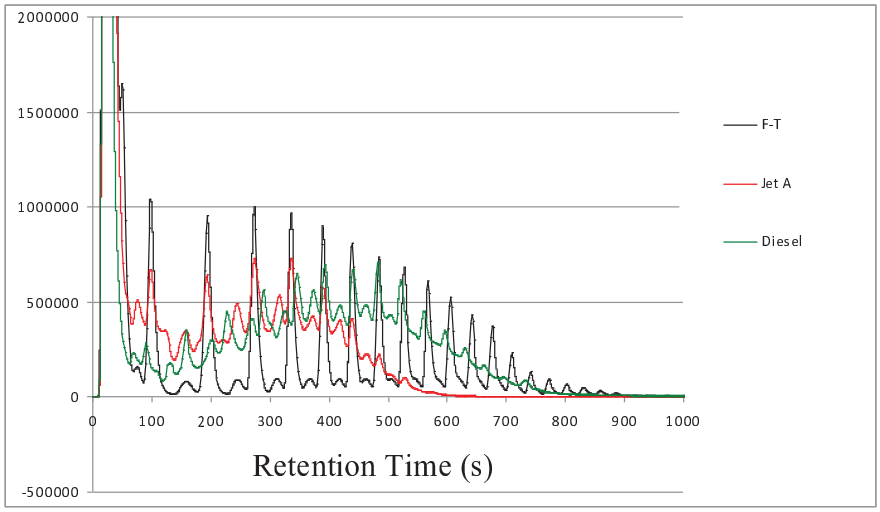

Figure 3.4: Gas chromatography results for liquid hydrocarbons

Work with the capillary reactor used a catalyst support that was 150 mesh TiO_2 in size and frequently plugged the reactor after a day or two of use. To avoid this problem, we tried a 2.0 mm tube packed with SiO_2 with a size of 30-60 mesh. We experienced less difficulty with plugging while maintaining the same product quality previously observed. In the next quarter we plan to explore larger diameter reactors to see if product quality can be maintained under less tightly controlled thermal conditions.

Though the 2.0 mm tube lasted long than the capillary reactor, problems with plugging still occurred. After a couple weeks of testing the reactor did develop a blockage due to compaction of the finer support particles. This reactor generated enough oil in a four hour run for GC testing but not enough to accurately measure water to oil ratios.

To obtain larger volumes, we constructed a new reactor with 0.25 inch diameter. Using the same SiO_2 support, we were able to run this reactor for a couple months without developing a blockage. This reactor produced liquid volumes on the order of milliliters for a day long experiment. We are now able to determine liquid product volume ratios through direct measurements. We also developed a method for measuring the volume flow rate of the outlet gases and also for collecting the gases for GC analysis. With this procedure we can now determine the composition of the outlet gases quantitatively.

A range of temperatures and pressures were explored in an effort to maximize the flow rate of liquid hydrocarbons. We found the larger diameter reactor maintains the product quality with slightly less controlled thermal conditions compared to the capillary reactor case.

In the last two quarters of the task, we developed and tested a reactor for methane reforming to syngas. The reactor consists of a heated steel reactor packed with Ni/Al_2O_3 catalyst. Calculations were performed to estimate the required space velocity, steam flow rates, and power input. A set of parametric experiments was design and performed to test the syngas gas composition as a function of steam and methane flow rates. An improved steam generator was constructed and replaced the one built in the previous quarter. The new generator is precisely regulates the amount of steam flowing into the reactor via a computer control system. Custom sample bags for hydrogen storage were used to take syngas samples. A GC-TCD was used to test the product gas composition.

Task 4: Bench-scale Modifications and Pilot Plant Design

Objectives:

1. Perform facility modifications to support the bench-scale integrated process
2. Following assessment of the integrated process, develop a requirements document for the laboratory scale pilot plant.
3. A laboratory-scale pilot plant conceptual design

Results:

Objective 1. Facility modifications were completed February 1, 2010 involving installation of benches, hoods, ventilation, electrical power, plumbing and service lines for lab space for this project. U.S. Representative Joe Barton, DOE Program Manager Paul Bakke and other dignitaries attended a grand opening on February 19, 2010. Facility has been in full use since then.

Objective 2. Following an assessment of the integrated process laboratory, requirements were developed for a scale 2000 bpd pilot plant.

Objective 3. A conceptual design of a pilot plant has been completed by Commonwealth Engineering, a design firm in Houston. A report was delivered in October 2010. The design includes capital cost estimates, process requirements and CAD drawings of a continuous closed loop pilot plant processing system that produces 2000 bbls of clean synthetic crude/day. Capital and operating cost estimates have also been made for 20,000 bpd, and 100,000 bpd. In the final quarter, we worked with Commonwealth Engineering for a scaled-up conceptual design for a coal cleaning operation to reduce the ash content of the Texas lignite. Modifications for adding a coal cleaning operation were completed in December 2011 by Commonwealth. The addition of this capability will significantly improve yields for lignite coals with more than 10% ash content.

Task 5: Project Management and Reporting

Objective: As part or all of the Task Descriptions, periodic reports and other deliverables will be provided in accordance with the Federal Assistance Reporting Checklist following the instructions included therein. The DoE project management personnel at the Golden Office will be consulted prior to initiation of the project work for specific requirements.

Current Status:

1. Final laboratory safety inspections were completed, and reports reported to the project manager.
2. All tasks, subtasks and milestones for this project were completed within established budgets.

Project Spending

Quarter	From	To	Estimated Federal Share of Outlays*	Actual Federal Share of Outlays	Estimated Recipient Share of Outlays*	Actual Recipient Share of Outlays	Cumulative
4Q 09	10/1/2009	12/31/2008	$747,452	$381,608	$200,865	$200,000	$581,608
1Q 10	1/1/2010	3/31/2010	$212,809	$ 16,062	$150,000	$150,000	$166,062
2Q 10	4/1/2010	6/30/2010	$443,203	$112,993	$0	$0	$112,993
3Q 10	7/1/2010	9/30/2010		$420,407	$0	$0	$420,407
4Q 10	10/1/2010	12/31/2010		$134,810	$0	$0	$134,810
1Q 11	01/1/2011	03/31/2011		$135,660	$0	$0	$135,660
2Q 11	04/01/2011	06/30/2011		$114,829	$865	$865	$115,694
3Q 11	07/01/2011	09/30/2011		$ 80,704	$0	$0	$ 80,704
4Q 11	10/01/2011	11/30/2011		$ 6,396			
Totals			**$1,404,537.76**	**$1,404,537.76**	**$350,865**	**$350,865**	**$1,755,402.76**